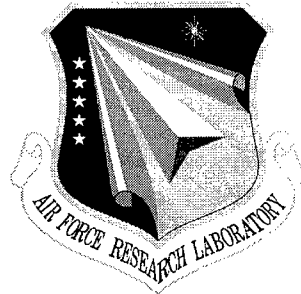


**RL-TR-97-255**  
**In-House Report**  
**April 1998**



# **OPTICAL NEURAL NETWORK CLASSIFIER ARCHITECTURES**

**Mark A. Getbehead, James B. Rosetti, Wesley E. Foor, Samuel P. Kozaitis**

*APPROVED FOR PUBLIC RELEASE; DISTRIBUTION UNLIMITED.*

**AIR FORCE RESEARCH LABORATORY  
ROME RESEARCH SITE  
ROME, NEW YORK**

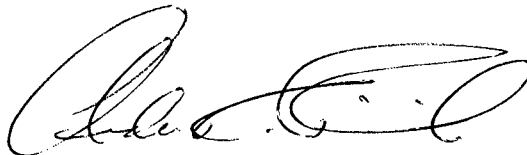
**DTIC QUALITY INSPECTED 3**

19980608 035

This report has been reviewed by the Air Force Research Laboratory, Information Directorate, Public Affairs Office (IFOIPA) and is releasable to the National Technical Information Service (NTIS). At NTIS it will be releasable to the general public, including foreign nations.

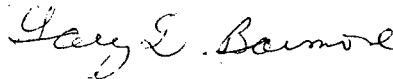
RL-TR-97-255 has been reviewed and is approved for publication.

APPROVED:



ANDREW R. PIRICH, Chief  
Photonics Processing Branch

FOR THE DIRECTOR:



GARY D. BARMORE, Maj, USAF  
Chief, Rome Operations Office  
Sensors Directorate

If your address has changed or if you wish to be removed from the Air Force Research Laboratory Rome Research Site mailing list, or if the addressee is no longer employed by your organization, please notify AFRL/SNDP, 25 Electronic Parkway, Rome, NY 13441-4515. This will assist us in maintaining a current mailing list.

Do not return copies of this report unless contractual obligations or notices on a specific document require that it be returned.

**REPORT DOCUMENTATION PAGE**

Form Approved  
OMB No. 0704-0188

Public reporting burden for this collection of information is estimated to average 1 hour per response, including the time for reviewing instructions, searching existing data sources, gathering and maintaining the data needed, and completing and reviewing the collection of information. Send comments regarding this burden estimate or any other aspect of this collection of information, including suggestions for reducing this burden, to Washington Headquarters Services, Directorate for Information Operations and Reports, 1215 Jefferson Davis Highway, Suite 1204, Arlington, VA 22202-4302, and to the Office of Management and Budget, Paperwork Reduction Project (0704-0188), Washington, DC 20503.

<b>1. AGENCY USE ONLY (Leave blank)</b>		<b>2. REPORT DATE</b> April 1998	<b>3. REPORT TYPE AND DATES COVERED</b> In-House Oct 96 - Sep 97	
<b>4. TITLE AND SUBTITLE</b> OPTICAL NEURAL NETWORK CLASSIFIER ARCHITECTURES			<b>5. FUNDING NUMBERS</b> C - N/A PE - 62702F PR - 4600 TA - P1 WU - 33	
<b>6. AUTHOR(S)</b> Mark A. Getbehead, James B. Rosetti, Wesley E. Foor (Air Force Research Lab) Samuel P. Kozaitis (Florida Institute of Technology)				
<b>7. PERFORMING ORGANIZATION NAME(S) AND ADDRESS(ES)</b> Air Force Research Laboratory/SNDP 25 Electronic Parkway Rome NY 13441-4515			<b>8. PERFORMING ORGANIZATION REPORT NUMBER</b>  RL-TR-97-255	
<b>9. SPONSORING/MONITORING AGENCY NAME(S) AND ADDRESS(ES)</b> Air Force Research Laboratory/SNDP 25 Electronic Parkway Rome NY 13441-4515			<b>10. SPONSORING/MONITORING AGENCY REPORT NUMBER</b>  RL-TR-97-255	
<b>11. SUPPLEMENTARY NOTES</b>  Air Force Research Laboratory Project Engineer: Mark A. Getbehead/SNDP/(315) 330-4146				
<b>12a. DISTRIBUTION AVAILABILITY STATEMENT</b>  Approved for public release; distribution unlimited			<b>12b. DISTRIBUTION CODE</b>	
<b>13. ABSTRACT (Maximum 200 words)</b> We present an adaptive opto-electronic neural network hardware architecture capable of exploiting parallel optics to realize real-time processing and classification of high-dimensional data for Air Force Hostile Target Identification (HTI). This architecture utilizes a grayscale-input radial basis function neural network based on a previously demonstrated binary-input version. The greyscale-input capability broadens the range of applications for the classifier by allowing it to handle 8 bit input data. We characterized a key component of this system, a variable phase retarder, and found that the phase uniformity changed less than 7% with applied voltage. An optical wavelet transform preprocessor is also discussed. The preprocessor produces a reduced feature set of multiwavelet images to improve training times and discrimination capability of the neural network. The design uses a joint transform correlator (JTC) to provide cross correlations of multiple input images. We present experimental results for a JTC which used four input images generated with a spatial light modulator. We then propose using wavelet functions as input images to perform a multiwavelet feature extraction. The results from the retarder characterization and optical wavelet transform work were to be used in a software simulation of the neural network system to determine its feasibility. However, this work remains unfinished as this project was canceled due to budget cuts.				
<b>14. SUBJECT TERMS</b> Optical Neural Networks, Radial Basis Functions, Pattern Recognition, Optical Wavelet Transform, Multiscale Image Processing			<b>15. NUMBER OF PAGES</b> 56	
			<b>16. PRICE CODE</b>	
<b>17. SECURITY CLASSIFICATION OF REPORT</b> UNCLASSIFIED	<b>18. SECURITY CLASSIFICATION OF THIS PAGE</b> UNCLASSIFIED	<b>19. SECURITY CLASSIFICATION OF ABSTRACT</b> UNCLASSIFIED	<b>20. LIMITATION OF ABSTRACT</b> UL	

## Abstract

We present an adaptive opto-electronic neural network hardware architecture capable of exploiting parallel optics to realize real-time processing and classification of high-dimensional data for Air Force Hostile Target Identification (HTI). This architecture utilizes a grayscale-input radial basis function neural network based on a previously demonstrated binary-input version. The greyscale-input capability broadens the range of applications for the classifier by allowing it to handle 8 bit input data. We characterized a key component of this system, a variable phase retarder, and found that the phase uniformity changed less than 7% with applied voltage. An optical wavelet transform preprocessor is also discussed. The preprocessor produces a reduced feature set of multiwavelet images to improve training times and discrimination capability of the neural network. The design uses a joint transform correlator (JTC) to provide cross correlations of multiple input images. We present experimental results for a JTC which used four input images generated with a spatial light modulator. We then propose using wavelet functions as input images to perform a multiwavelet feature extraction. The results from the retarder characterization and optical wavelet transform work were to be used in a software simulation of the neural network system to determine its feasibility. However, this work remains unfinished as this project was canceled due to budget cuts.

---

## Acknowledgments

The authors wish to acknowledge members of the Photonics center for their support and technical inputs. The authors acknowledge Andy Pirich for his encouragement and Joanne Rossi for her invaluable administrative support.

All authors contributed to the work presented in this report. Mark A. Getbehead wrote sections of this report and edited and assembled the overall document. He also worked on the setup and testing of the optical wavelet preprocessor. Jim B. Rosetti performed the phase retarder characterization experiments and wrote the associated chapter in this report. Wesley E. Foor, who has since left the Photonics Center, was the guiding force behind this project. He performed the binary-input classifier work and wrote the related chapter in this report. Dr. Samuel P. Kozaitis developed the initial design for the optical wavelet preprocessor and worked on its fabrication and testing. He also contributed to this report.

# Table of Contents

Abstract.....	i
Acknowledgments.....	ii
List of Figures.....	iv
List of Tables.....	v
1. Introduction .....	1
2. Binary Input Neural Network Classifier .....	4
2.1 Radial Basis Function Neural Networks .....	4
2.2 Previous Results.....	6
2.3 Optical RBF Neural Network .....	6
2.3.1 Parallel Optical Distance Computation .....	7
2.3.2 Parallel Basis Function Evaluation .....	8
2.3.3 Overview of Previous Results from a System Noise Analysis .....	8
2.4 Adaptive Optical Radial Basis Function Neural Network.....	9
3. Grayscale Input Neural Network Classifier .....	11
3.1 Optical Image Subtraction .....	11
3.2 Retardance Uniformity of the Meadowlark Optics Liquid Crystal Variable Retarder .....	11
3.2.1 Theory of Operation.....	13
3.2.2 Procedure .....	14
3.2.3 Results.....	14
3.2.4 Conclusions.....	18
4. Optical Wavelet Preprocessing .....	19
4.1 Conventional joint-transform correlator.....	19
4.2 Multiple-input joint transform correlator .....	20
4.3 Experimental results with the multiple-input JTC.....	21
4.4 Multiwavelet feature extraction .....	21
4.4.1 Wavelet transform.....	21
4.4.2 Multiwavelet analysis.....	22
4.4.3 Simulation .....	23
4.4.4 Implementation .....	24
4.5 Results.....	25
5. Conclusion .....	39
6. References.....	41

# List of Figures

Figure 2.1: Schematic diagram of RBF neural network for digit recognition. ....	5
Figure 2.2: Dual-rail vector-matrix multiplier used as a parallel optical distance computer.....	7
Figure 2.3: Non-adaptive RBF postprocessing chip for a single-output network. ....	9
Figure 2.4: Adaptive RBF postprocessing chip module.....	10
Figure 3.1: Optical image subtracter using phase-shifter .....	12
Figure 3.2: Optical image subtracter used as a grayscale-input parallel distance computer.....	12
Figure 3.3: Retarder used as an attenuator .....	14
Figure 3.4: Experiment Setup .....	15
Figure 3.5: Optical Power Vs. Applied Voltage .....	15
Figure 3.6: Phase Uniformity at 2V .....	16
Figure 3.7: Phase Uniformity at 3V .....	17
Figure 3.8: Phase Uniformity at 4V .....	17
Figure 3.9: Phase Uniformity at 10V .....	18
Figure 4.1: Schematic diagram of a conventional joint-transform correlator.....	26
Figure 4.2: Input plane of multiple-input JTC. ....	27
Figure 4.3: Output plane of multiple-input JTC.....	27
Figure 4.4: Experimental set-up of multiple input JTC.....	28
Figure 4.5: Input image used in experiment.....	29
Figure 4.6: Input image used in experiment.....	29
Figure 4.7: Left hand side of output plane obtained experimentally when Figure 4.5 was used as the input plane intensity distribution.....	30
Figure 4.8: Left hand side of output plane obtained experimentally when Figure 4.5 was used as the input plane intensity plot of x axis. ....	30
Figure 4.9: Input plane for multiwavelet processing two wavelet scales. ....	31
Figure 4.10: Input plane for multiwavelet processing three wavelet scales. ....	31
Figure 4.11: Output plane for multiwavelet processing two wavelet scales.....	32
Figure 4.12: Output plane for multiwavelet processing three wavelet scales.....	32
Figure 4.13: Center portion of input plane used in simulation experiments.....	33
Figure 4.14: Output of multiwavelet simulation power spectrum. ....	33
Figure 4.15: Output of multiwavelet simulation output plane.....	34
Figure 4.16: Center portion of output plane thresholded at three different values showing the overlap of correlation responses. ....	35

Figure 4.18: Close-up view of left hand side of Fig. 11. Response on left is for  $a_2=1.2$  response on right is for  $a_1 + a_2$ , where  $a_1 = 1.0$ . ..... 37

Figure 4.19: Schematic diagram of multiple-input JTC used for multiwavelet analysis..... 38

## List of Tables

Table 3.1: Accuracy of Measurements..... 16

Table 3.2: Minimum and Maximum Retardance Values ..... 16

# 1. Introduction

Adaptive neural networks are considered to be promising architectures for real-time pattern recognition. Due to the large network sizes required for real-world problems involving imagery, these adaptive networks will be most useful for solving real-time problems if they are implemented in parallel hardware. The parallel processing capabilities of opto-electronic systems together with the relatively simple computational requirements of artificial neural networks make optics a natural candidate for hardware implementations of neural computing systems. Optical computing systems however, typically suffer from optical device imperfections and system noise that can degrade performance. By employing adaptive on-line training techniques these noise sources can be incorporated into an error-driven learning process to provide improved system performance. Neural networks therefore offer an opportunity to realize parallel optical computing systems that tolerate noise.

The radial basis function (RBF) neural network has been successfully used in many multi-dimensional classification applications including 3D object recognition,<sup>1,2</sup> radar signal classification,<sup>3</sup> face recognition,<sup>4,5</sup> fingerprint recognition<sup>6</sup>, speech recognition,<sup>7</sup> and handwritten character recognition.<sup>8,9,10</sup> Other applications of RBF neural networks include nonlinear function approximation,<sup>11, 12, 1</sup> kernel regression<sup>13</sup>, 'neural beamforming' for phased-array antennas,<sup>14,15,16,17</sup> equalization of time-dispersive communication channels, and nonlinear modeling and prediction for echo cancellation in the presence of nonlinear distortion.<sup>18</sup> Previous experiments have shown that RBF networks have similar classification performance to backpropagation neural networks while typically incurring shorter training times.<sup>8</sup> Both all-electronic<sup>19</sup> and opto-electronic<sup>20,10</sup> parallel hardware implementations of RBF networks have been reported.

An important extension of current RBF networks, and a major topic in this report, is the development of an optical RBF network classifier permitting analog and complex valued input signals. One particular application of a complex-input system is radar direction finding. A new antenna beamforming approach 'neural beamforming', has been developed at Air Force Research Laboratory by researchers Major Jeffrey Simmers and Dr. Hugh Southall of RL/ERAS and Terry O'Donnell from the ARCON Corporation.<sup>14,15,16,17</sup> Their goal is to design neural processing algorithms that can adapt to low cost phased-array antennas, even if the antennas behave in a nonlinear manner, are imperfectly manufactured, or become degraded after some period of time. Neural beamforming techniques can decrease antenna manufacturing and maintenance costs and increase mission time and performance between repair actions. The group is now beginning to search for parallel processing hardware in order to meet this signal processing demand. The analog adaptive optical RBF classifier system, described in this report, may present a viable solution to this large, real-time problem.

The training time of a neural network can be decreased by reducing the size of the feature set. In addition, the quality of features input to the neural network will influence

its recognition rate. In applications using focal plane imagery, the image pixels can be used as features. However, image pixels are typically numerous and form an unnecessarily large feature set.

Image edges are a more compact feature set than image pixels. Edges represent important image features like object boundaries and textures. Multiscale edge features are required to represent objects and textures of different sizes.<sup>21</sup> Wavelet transforms, currently popular in signal processing, perform a multiscale or multiresolution analysis of an image. The resulting wavelet representation contain edge features at multiple scales. We can extract multiple wavelet-scale version of an image with an optical imaging system based on the joint-transform correlator (JTC).

The main difference between a JTC and a conventional Vanderlugt (4f) correlator is that the images in the JTC are encoded in the spatial domain. In terms of their output, both types of correlators perform the same operation, the cross-correlation between two images. In a 4f correlator, the Fourier transform of an input image is imaged onto the Fourier transform of a reference image. In a JTC, both input and reference images are input simultaneously in the spatial domain, then the Fourier transform is performed. The JTC has certain advantages when compared to the 4f correlator such as ease of alignment and avoiding spatial filter synthesis.<sup>22,23</sup>

Although most configurations of the JTC use two input images, the use of multiple input images may allow additional functions to be performed. For example, an image and two different wavelets were used in a JTC for multispectral (multiwavelet) wavelet feature extraction of the image.<sup>24</sup> In this approach, different versions of an input image corresponding to different wavelet scales appeared at different locations in the output plane. Another JTC configuration used three inputs, but required an additional electronic optical processing step to implement the wavelet transform.<sup>25</sup> Another approach used two SLMs with holographic mask to produce a wavelet-based JTC.<sup>26</sup> In addition, a JTC was used with a single reference image and multiple inputs,<sup>27</sup> and color pattern recognition was achieved with a multichannel approach.<sup>28</sup> Although the wavelet transform has provided an application for a JTC with multiple inputs<sup>29</sup>, a generalized JTC with multiple inputs may find more applications including those in other areas if its output function was properly described.

One goal of this project was to develop an optical wavelet preprocessor. This preprocessor design uses a JTC to extract multiscale features from an input image and provide these features to an optical RBF classifier.

In this report, we begin in Chapter 2 by reviewing theory of adaptive radial basis function neural networks. We then describe the architecture for a optical RBF classifier that facilitates on-line learning to offer robustness to noise and optical system imperfections. In Chapter 3, we propose a grayscale-input data classifier for use with non-binary (8 bit or analog) signals. We then present results of the characterization of a variable retarder to be used for the image subtraction. In Chapter 4, we describe ongoing

work in the development of a multiscale optical wavelet transform system intended for use as an image preprocessor for the classifier. The general theory of a conventional JTC is presented then extended to a multiple input JTC. We show experimental results for a joint transform correlator which used four input images generated with a spatial light modulator. We then describe how a multiple-input JTC can be used for multiwavelet analysis and propose an architecture that has the same space-bandwidth product as a two-input JTC. Finally, in Chapter 5, we present conclusions and future directions for this work.

## 2. Binary Input Neural Network Classifier.

In this chapter we briefly describe a binary-input data optical radial basis function (RBF) neural network classifier. Many classifier applications either use binary data directly or may be converted to a binary data format with acceptable degradation including: optical character recognition, fingerprint identification, (edge-enhanced) template matching, and certain disparity computations. More details of this binary-input system design and its application to handwritten digit recognition can be found in earlier publications<sup>10,30</sup> and also in our report from a previous project.<sup>31</sup>

### 2.1 Radial Basis Function Neural Networks

A single-output multilayer neural network can be regarded as a continuous input-output mapping,  $\mathcal{R}^N \rightarrow \mathcal{R}$ . The network should behave well in the presence of noise and correctly generalize when a previously unseen input pattern is presented. To obtain these characteristics we may impose smoothing constraints on the input-output mapping as derived from regularization techniques and approximation theory.<sup>1</sup> Approximation theory attempts to provide an optimal solution to approximating a continuous multivariate function  $f(\mathbf{x})$ , with an *approximating function*  $\hat{f}(w, x)$ , where  $\mathbf{x}$  is a  $N$  dimensional input vector and  $\mathbf{w}$  is a parameter vector used to minimize the approximation error. The set of  $M$  input vectors comprise the training set on which the desired input-output mapping,  $\{\mathbf{x}_i \rightarrow f(\mathbf{x}_i) ; i = 1, \dots, M\}$ , is defined.

The RBF approximation scheme arises when certain symmetry assumptions are made about the smoothing constraints utilized in the regularized solution and corresponds to an approximating function of the form

$$\hat{f}(w, x) = \sum_{i=1}^M a_i \exp\left(\frac{-|\mathbf{x} - \mathbf{t}^i|^2}{\sigma_i^2}\right), \quad (2.1)$$

where  $\{\mathbf{t}^i\}$  is a set of center locations,  $\{\sigma_i\}$  are the corresponding center widths, and  $\{a_i\}$  are a set of weighting factors. These three sets define the parameters of  $\mathbf{w}$ .

The approximation function given above can be represented in the form of a one-layer neural network as shown in Figure 2.1. The hidden layer RBF node response is given by

$$y_i = \exp\left(\frac{-|\mathbf{x} - \mathbf{t}^i|^2}{\sigma_i^2}\right), \quad (2.2)$$

where  $\mathbf{t}^i$  is the neuron center and  $\sigma_i$  is the neuron width. In contrast to conventional networks, which use inner products, the first layer requires the calculation of a Euclidean distance. In addition, the neuron response is not sigmoidal but corresponds to a  $\exp(-x^2/\sigma^2)$  function. For a multiple-output RBF network, the  $k^{th}$  output node response to an input vector  $\mathbf{x}$  is given by

$$f_k(x) = \sum_{i=1}^M a_{ik} \exp\left(\frac{-|\mathbf{x} - \mathbf{t}^i|^2}{\sigma_i^2}\right), \quad (2.3)$$

where  $a_{ik}$  is the connection weight between the  $i^{th}$  RBF node and the  $k^{th}$  output node. A class-based clustering algorithm was applied to the training set to improve the first layer hardware efficiency and to eliminate redundant center locations.<sup>10</sup>

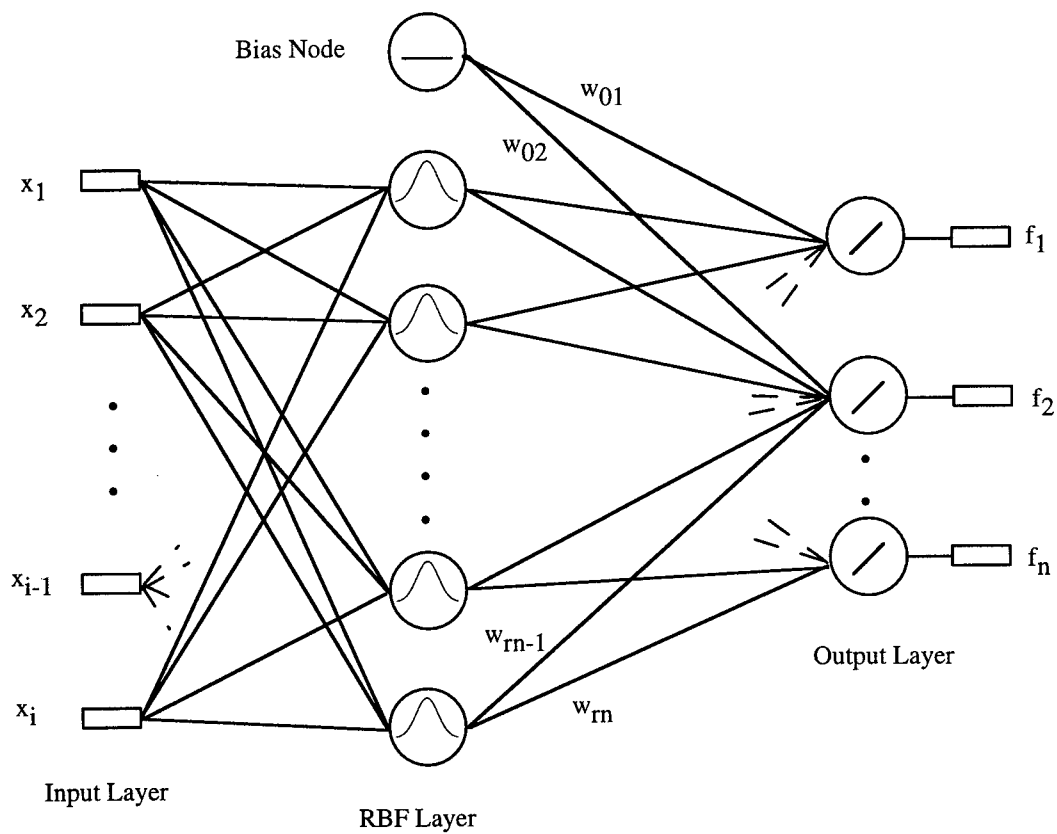


**Figure 2.1:** Schematic diagram of RBF neural network for digit recognition.

One can train parameters  $\{\sigma_i\}$  and  $\{a_{ik}\}$  by minimizing the squared error at each output node, using a gradient descent technique. The squared error of the  $k^{\text{th}}$  output node in the presence of the single input vector  $\mathbf{x}^l$  is defined as

$$(E_k^l)^2 = [\hat{f}_k(\mathbf{w}, \mathbf{x}^l) - f_k(\mathbf{x}^l)]^2.$$

The gradient descent update equation for the  $p^{\text{th}}$  RBF width is

$$\Delta\left(\frac{1}{\sigma_p^2}\right) = -\alpha_\sigma (E_k^l)^2 \left(|\mathbf{x}^l - \mathbf{t}^p|^2\right) a_p \exp\left(\frac{-|\mathbf{x}^l - \mathbf{t}^p|^2}{\sigma_p^2}\right), \quad (2.4)$$

where  $\alpha_\sigma$  is the acceleration constant for the width update. The update equation for the interconnection weight between the  $p^{\text{th}}$  RBF node and the  $k^{\text{th}}$  output node is

$$\Delta(a_{pk}) = \alpha_a (E_k^l)^2 \exp\left(\frac{-|\mathbf{x}^l - \mathbf{t}^p|^2}{\sigma_p^2}\right), \quad (2.5)$$

where  $\alpha_a$  is the acceleration constant for the weight update. The iterative update equations are applied after each training input vector is presented.

## 2.2 Previous Results

In previous work, we used handwritten digit recognition to evaluate the performance of our RBF neural network classifier.<sup>31</sup> We trained and tested a software version of the network described above. The best results obtained were 100.0% recognition of the training set and 97.7% correct recognition of the testing set data. These recognition rates serve as a baseline for evaluating the performance of future optical RBF neural network designs.

## 2.3 Optical RBF Neural Network

Here we describe an optoelectronic implementation of a parallel RBF neural network classifier. The hardware implementation of the RBF classifier is composed of two subsystems; the first is a parallel Euclidean distance computer, which we implement in optics. This subsystem is spatially multiplexed and makes use of two-dimensional SLM's to represent the center locations. The second subsystem evaluates the basis functions and performs the interconnect weighting between the RBF layer and the output layer. An electronic hardware design is proposed for implementing the postprocessing subsystem.

In our system the optically computed distances are captured with a CCD camera and the postprocessor is simulated in software.

### 2.3.1 Parallel Optical Distance Computation

The first layer of the RBF neural network computes the Euclidean distance between the input and each of the centers. The Euclidean distances  $\{d^i\}$ , between vector  $\mathbf{x}$  and the centers  $\{\mathbf{t}^i\}$ , can be written as

$$d^i = |\mathbf{x} - \mathbf{t}^i|^2 = \sum_{j=1}^N (x_j - t_j^i)^2 = \sum_{j=1}^N d_j^i, \quad (2.6)$$

where

$$\bar{d}_j^i = x_j t_j^i + \bar{x}_j \bar{t}_j^i, \quad (2.7)$$

for the case of binary vectors. The overbar indicates a bitwise complement. We can implement this distance computation in parallel hardware by using the optical system shown in Figure 2.2. This system is spatially multiplexed, in contrast with previously demonstrated time-multiplexed optical disk-based systems.<sup>20,32</sup> The light in *LEG 1* of the system illuminates the input SLM, labeled  $\mathbf{x}$  and is then collimated in the  $y$  direction and imaged in the  $x$  direction onto the centers SLM, labeled  $\mathbf{t}_j^i$ . The result that appears immediately behind the centers SLM is the product term  $\{x_j t_j^i ; i=1, \dots, M; j=1, \dots, N\}$ ,

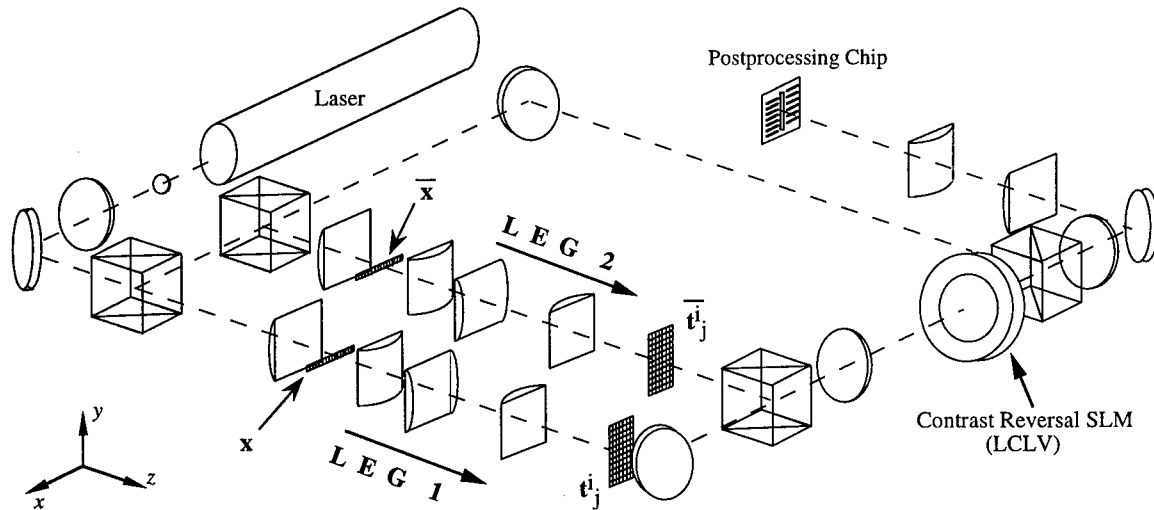


**Figure 2.2:** Dual-rail vector-matrix multiplier used as a parallel optical distance computer.

which is required in the distance computation. *LEG 2* of the system forms the products

$$\{\bar{x}_j, \bar{t}_j^i\}$$

in a similar fashion. The results of these vector-matrix multipliers are simultaneously imaged onto a contrast-reversing liquid-crystal light valve (LCLV) SLM, where they are superimposed to form the terms  $\{\bar{d}_j^i\}$ . The result of the contrast reversal yields the  $\{d_j^i\}$  terms and the final integration operation  $\sum_{j=1}^N d_j^i$ , is performed with a cylindrical lens. For real-time operation, electronically addressed one-dimensional SLM's would be used for the  $x$  and  $\bar{x}$  inputs.

The accuracy of the optical distance computation and its influence on classification rate were quantified in a previous effort.<sup>22</sup> It was found that the average rms error for the optical distance computation over the testing set of handwritten digits was 29%. The large magnitude of this error lead us to believe that we would have a large classification error in our system. The errors in the optical distance computation were due to device imperfections and system noise.

The optically computed distances were fed into a simulation of the radial basis function (RBF) neural network to determine the overall recognition rate for the optical classifier. The resulting recognition rate of 31.0% was very poor. It did not agree with the 97.7% testing recognition rate from the RBF network simulations reported in Section 2.2. It was evident that the distance errors caused by the optical system imperfections had a catastrophic effect upon the overall system performance.

### 2.3.2 Parallel Basis Function Evaluation

We now consider the second subsystem of the RBF classifier, which performs the basis function evaluation and output interconnect weighting. The block diagram in Figure 2.3 shows a possible electronic implementation of the subsystem for the single output case.<sup>20</sup> Each array of 198 modules provides a single network output; therefore, we require ten such arrays for our application. Note that all of the proposed operations are local, with exception of the global sum, and are compactly achievable in analog VLSI circuitry. It is also possible, however, that digital techniques would be desirable in order to increase processing speed and/or accuracy within the postprocessor. In this nonadaptive postprocessor the network center widths and interconnection weights can be trained off line in software and then downloaded to the chip during operation. In our current neural network the electronic postprocessor chip is emulated in software.

### 2.3.3 Overview of Previous Results from a System Noise Analysis

To determine why the optical distance computation and consequently the recognition rate were so bad, we performed a noise analysis of the optical RBF system in a previous effort.<sup>22</sup> This was done using a detailed computer model that used parameters taken from the actual optical hardware. The noise terms that were incorporated in the model included optical system imperfections (illumination nonuniformities, input and centers SLM finite contrast, and optical system point-spread function), LCLV response

(intensity transfer function and spatial resolution), and detector response (analog-to-digital quantization error and detector random noise). Each noise term was characterized in terms of its effect on the optical distance computation. The model performed well as it produced a recognition rate of 28.0% vs. 31.0% for the actual optically computed data. Simulation results indicated the liquid crystal light valve, used for contrast reversal, was the primary error source in the system.

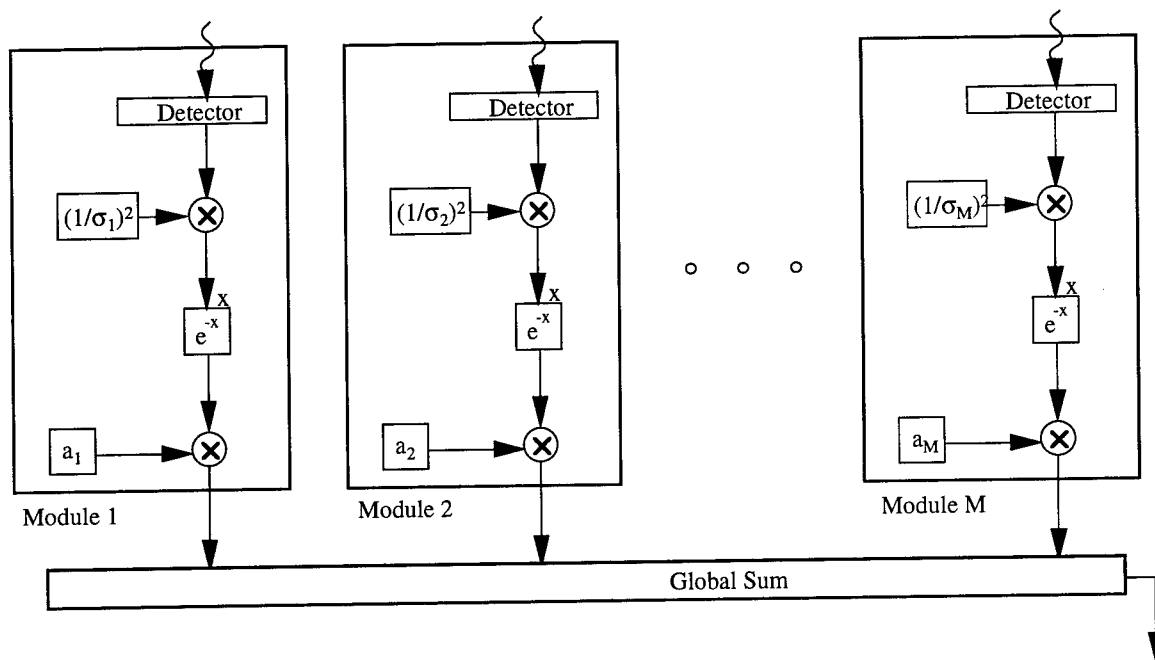


**Figure 2.3:** Non-adaptive RBF postprocessing chip for a single-output network.

## 2.4 Adaptive Optical Radial Basis Function Neural Network

As we have seen in Section 2.3, our optical hardware network performance greatly suffers because of errors in distance computation caused by optical system imperfections and noise. We expect that by training our optical system in the presence of these imperfections, the network will compensate for these errors and its performance will more closely match that of the software RBF network. In this section we consider an adaptive postprocessor.<sup>20</sup>

By modifying the non-adaptive single-output postprocessor presented in Section 2.3, we can incorporate error feedback in order to implement on-line network training. Using the electronic module shown in Figure 2.4, we can directly implement the gradient descent update Equations (2.4) and (2.5). In addition to error feedback for each module, we also require accumulation registers for adapting both the RBF widths and weights in an iterative fashion. As in the non-adaptive case we require ten arrays, each consisting of

198 modules for the optical fully-parallel implementation of the digit recognition RBF network shown in Figure 2.1.

Simulation results indicated that on-line training compensated for optical imperfections and errors and significantly improved the performance of the classifier. Using the actual optically computed testing distances together with the on-line learning gave a final recognition rate of 92.67%. The adaptive optical system provided almost a 60% increase in recognition performance as compared with the non-adaptive optical RBF classifier. Therefore there is a significant improvement imparted by adaptive on-line training.

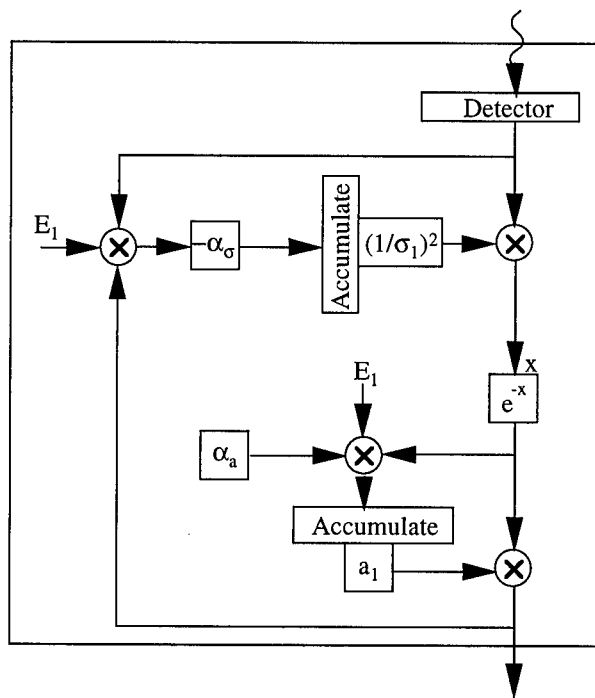


**Figure 2.4:** Adaptive RBF postprocessing chip module.

### 3. Grayscale Input Neural Network Classifier

In this chapter we describe a design for a grayscale input distance computer for use with our RBF classifier. We show that by modifying the distance computation optics of the binary classifier system we can develop a grayscale input capable classifier. In essence we replace the XOR functions with optical image subtraction optics. In this chapter, we briefly present an appropriate optical image subtraction method. Next, we present characterization results for a liquid crystal variable retarder we plan to employ in our system.

#### 3.1 Optical Image Subtraction

Because of its simplicity we chose to perform the real-time image subtraction by a phase shifting method<sup>33</sup>, rather than by Fourier methods<sup>34,35</sup> or electrooptic (via SLMs) effect methods.<sup>36</sup> Reviews of optical image subtraction techniques are given in Ebersole<sup>33</sup> and Liu and Chao.<sup>37</sup>

In a coherent optical system, the simplest way to achieve image subtraction is by a phase shifting method. As shown in Figure 3.1, two paths are split from a single coherent source and each illuminates an image. A phase plate or variable phase retarder is placed in one of the two paths to create a phase delay of  $\pi$  which multiplies the image in that path by  $e^{i\pi} = -1$ . The image subtraction is completed when the two paths are added together in the combining beamsplitter. The detector array (i.e., postprocessing chip) detects the magnitude of the amplitude image subtraction, which is our desired distance measure.

The Euclidean distances  $\{d^i\}$ , between the input vector  $\mathbf{x}$  and the centers  $\{t^i\}$ , can be directly computed as  $d^i = |\mathbf{x} - t^i|^2$ . We make use of a variable phase retarder in order to easily adjust the phase delay without disturbing the position of the mounted optical components. The capability of phase delay adjustments also permits us to perform software error analysis over a wide operating range. We begin by characterizing the liquid crystal variable retarder to be used in our system.

#### 3.2 Retardance Uniformity of the Meadowlark Optics Liquid Crystal Variable Retarder

In this section, we characterize the Meadowlark Optics liquid crystal variable retarder. The objective is to measure the uniformity of retardance across its aperture. In previous experiments we measured the amount of retardance the device produced as a function of voltage.<sup>31</sup>

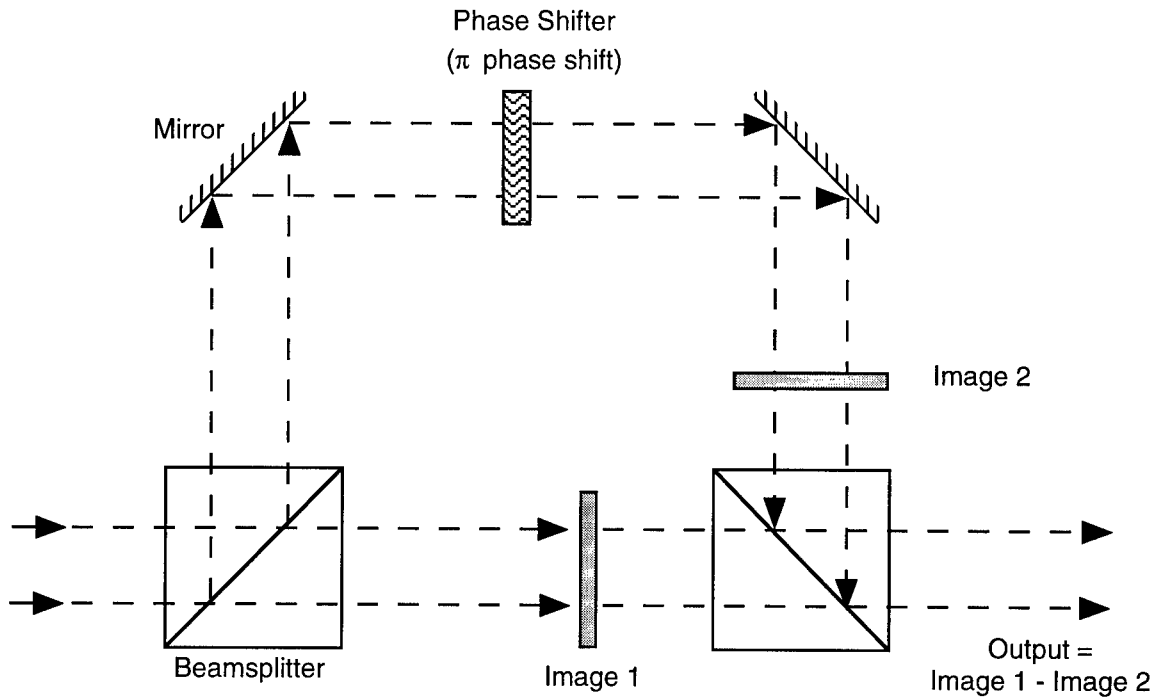


**Figure 3.1:** Optical image subtractor using phase-shifter.

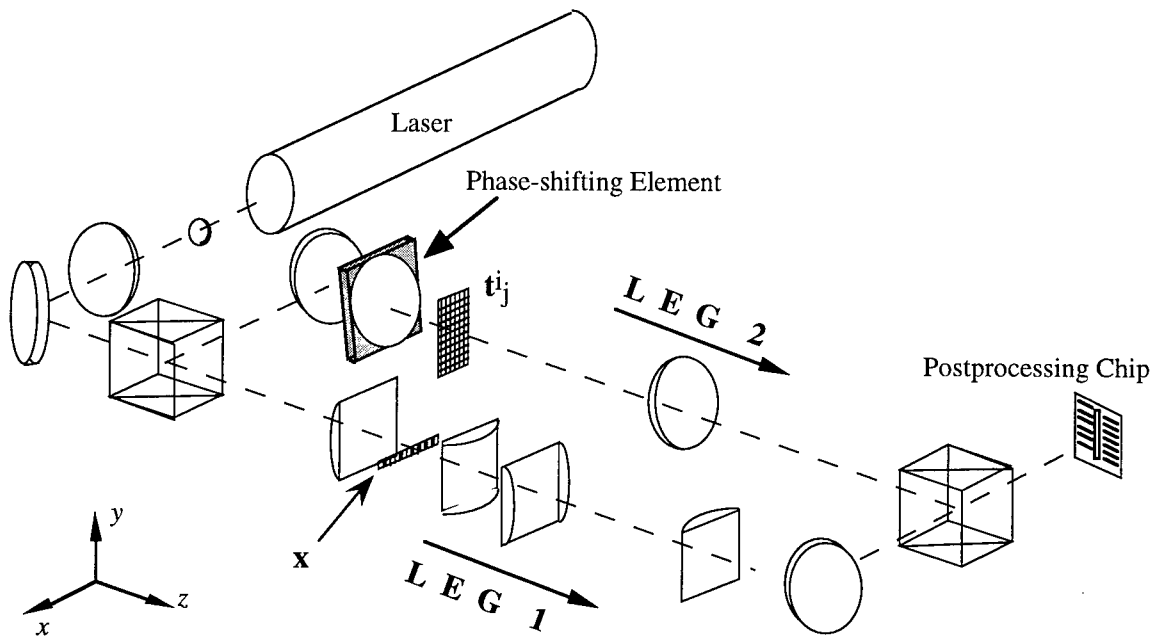


**Figure 3.2:** Optical image subtractor used as a grayscale-input parallel distance computer.

### 3.2.1 Theory of Operation

The retarder operates on the principle of birefringence. Birefringence is the property where a material exhibits two different indices of refraction along two different optical paths. These refractive indices are termed the ordinary refractive index,  $n_o$ , and extraordinary refractive index,  $n_e$ . Recall the equation for the speed of light,  $v$ , traveling through some material is

$$v = c/n, \quad (3.1)$$

where  $c$  is the speed of light in a vacuum, and  $n$  is the index of refraction parallel to the axis of polarization of the light. For the type of material used in this retarder,  $n_e > n_o$ , and thus  $n_e$  is termed the slow axis and  $n_o$  is termed the fast axis. Light polarized parallel to the slow axis travels slower than light polarized parallel to the fast axis.

The retarder consists of a liquid crystal material sandwiched between two glass windows. Each of these windows has a layer of optically transparent, electrically conductive indium tin oxide (ITO) applied. The liquid crystal is a birefringent material whose birefringence is dependent upon the alignment of the liquid crystal molecules. This alignment can be changed by applying an electric field, via the ITO, which changes the orientation of the molecules. The long axis of the molecules determines the slow axis, and with no electric field applied, the molecules lie parallel to the glass windows and exhibit a maximum index of refraction,  $n_e$ . When an electric field is applied, the molecules start to align themselves with the field which decreases  $n_e$ , and thus decreases the amount of birefringence.

To demonstrate a use of the retarder, assume linearly polarized light, whose axis of polarization is aligned between the fast and slow axis of the birefringent material, is incident on the retarder. This causes the phase of one orthogonal component of the light to lag the other which changes the polarization of the light. By varying the electric field, one can obtain various output polarizations. These polarizations range from linear to elliptical to circular, depending on how much one orthogonal component is lagged behind the other. This change in polarization can be used to make the device act as a variable attenuator by placing a polarizer and analyzer before and after the device, respectively. If the incident light's axis of polarization is 45 degrees from the slow (or fast) axis of the retarder (Figure 3.3), the resulting transmittance,  $T$  is the following function of retardance,  $R$ :

$$T = \sin^2\left(\frac{R}{2}\right). \quad (3.2)$$

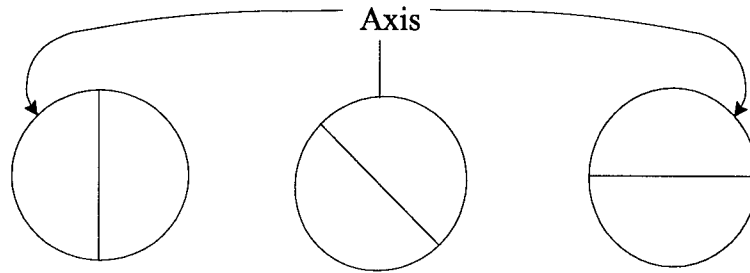


**Figure 3.3:** Retarder used as an attenuator

Another use of the retarder is to adjust the optical path length of light. If one aligns the axis of polarization of linearly polarized light to the slow axis of the retarder, that polarization will undergo a phase change caused by  $n_e$ . Thus, varying  $n_e$  by applying an electric field across the liquid crystal material, one can dynamically adjust the optical path length. This is how the retarder is to be used in the experiment.

### 3.2.2 Procedure

The uniformity measurements are made using the principle described in “Theory of Operation” and shown in 3.3. The setup used is shown in Figure 3.4. The beam splitter and optical power meter A are used to monitor any fluctuations in the laser’s output power in order to compensate for it. The resulting amplitude measured by the optical power meter B is a sine squared function of the retardance. Translating the device across the incident laser will give a profile of the retardance.

The device was mounted on two Klinger programmable translation stages. The stages were moved 2 mm in each axis. A 10 by 10 array of data points was collected across the face of the device at four different applied voltages (retardances). This was repeated 10 times (runs) to ensure data integrity. The four different voltages were chosen to allow enough optical power to reach the detector (to reduce sensitivity to noise) and to give an adequate sample across the operating voltages of the device (see Figure 3.5). The retardance was then calculated and graphed. For each voltage, the standard deviation of each array point of the 10 runs was calculated to make sure the data was valid.

### 3.2.3 Results

For each array point across the aperture, the standard deviation was calculated using the values for all ten runs. Table 3.1 shows the maximum standard deviation found. Also is shown the retardance of that data point, averaged across the ten runs.

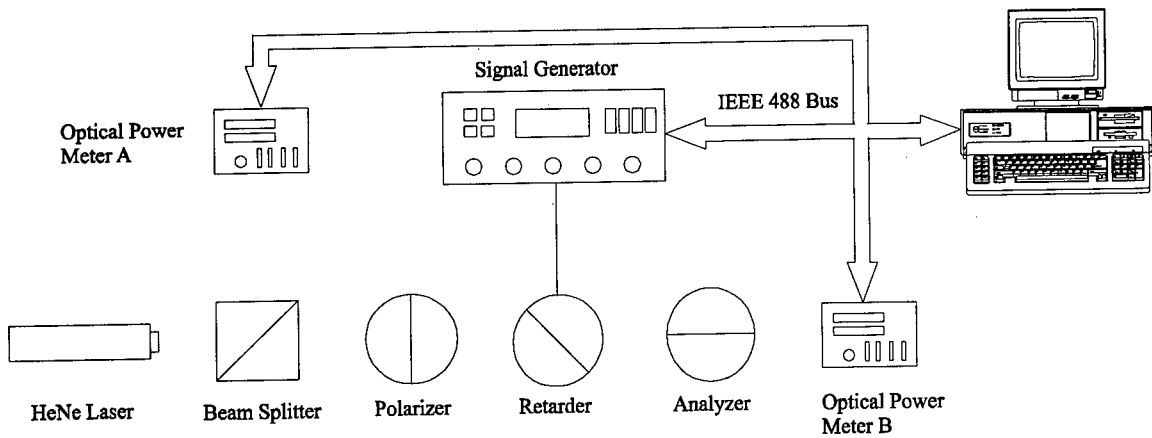


**Figure 3.4:** Experiment Setup

**Optical Power Vs. Voltage**

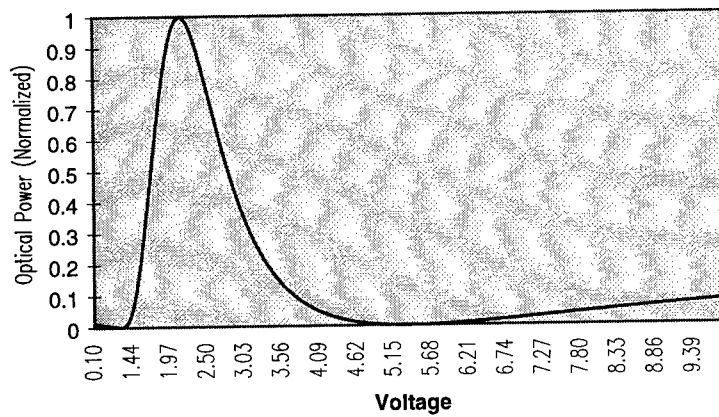


**Figure 3.5:** Optical Power Vs. Applied Voltage

	2 Volts	3 Volts	4 Volts	10 Volts
Average Retardance (radians)	2.54	1.34	0.527	0.527
Maximum Standard Deviation	0.0417	0.0110	0.00822	0.00134

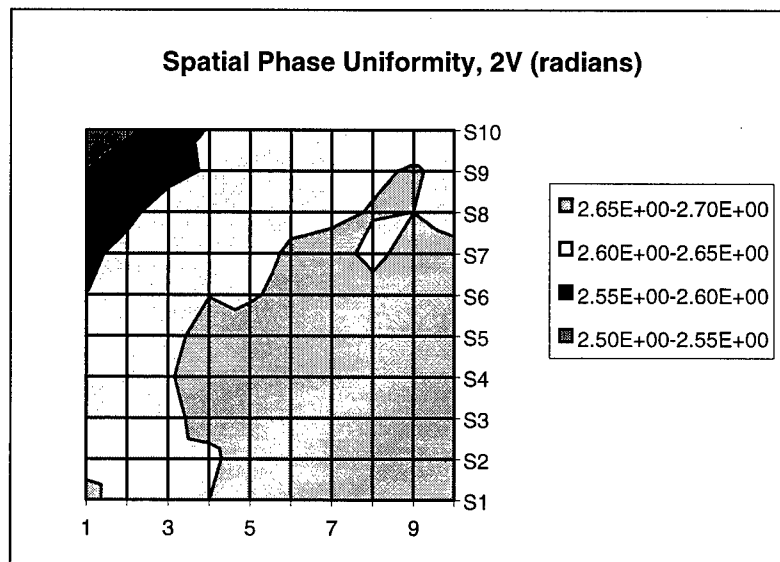
**Table 3.1:** Accuracy of Measurements.

Table 3.2 shows minimum and maximum phase retardance found for one data run which is typical of the other nine runs. Note, the average retardance in this table refers to the average of the 100 data points for this run only (not to be confused with the averages in Table 3.1). This table shows the retardance varies across the aperture no more than seven percent.

	2 Volts	3 Volts	4 Volts	10 Volts
Minimum Retardance	2.54	1.32	0.513	0.495
Maximum Retardance	2.70	1.40	0.574	0.543
Average Retardance	2.65	1.36	0.537	0.527

**Table 3.2:** Minimum and Maximum Retardance Values

Figures 3.6 through 3.9 are graphs of this run. These graphs show how the phase varies spatially across the aperture for each applied voltage.



**Figure 3.6:** Phase Uniformity at 2V

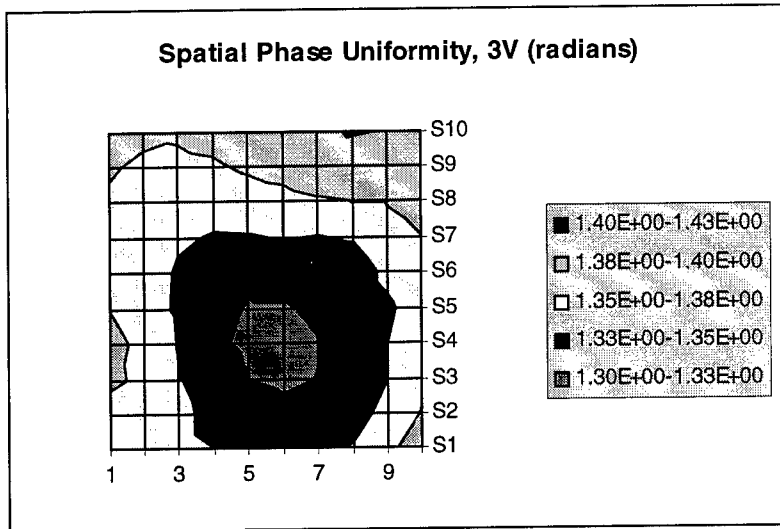


**Figure 3.7:** Phase Uniformity at 3V

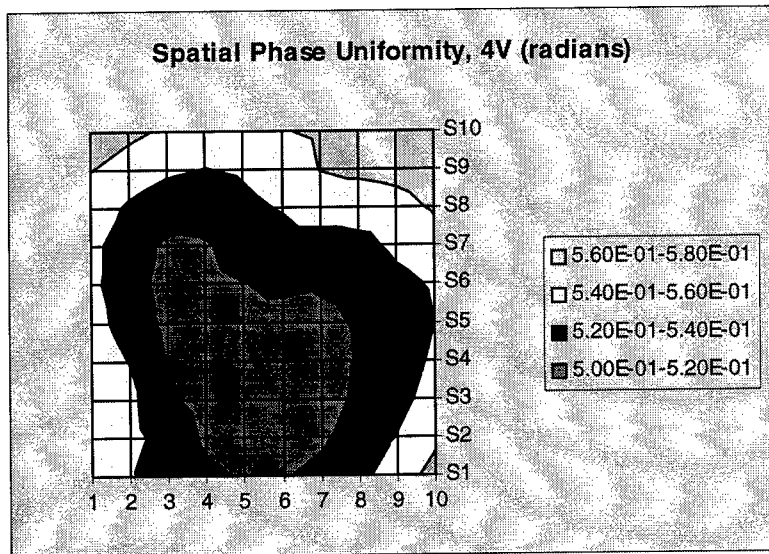


**Figure 3.8:** Phase Uniformity at 4V

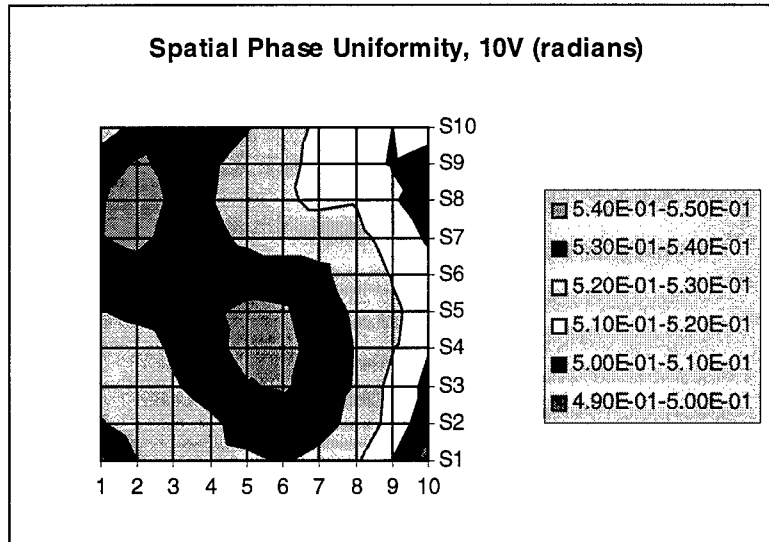


**Figure 3.9:** Phase Uniformity at 10V

### 3.2.4 Conclusions

The spatial phase uniformity does appear to change with different voltages applied. However, the difference is not large (less than seven percent). The project was canceled before these results could be fed into a simulation of the neural network to see what impact this small variation would have. If it would adversely affect the operation of the network, a more complete characterization of the device would be required.

## 4. Optical Wavelet Preprocessing

In this chapter we present an imaging system, based on the joint transform correlator (JTC), that produces a multiple wavelet-scale features from an input image. This system could be used as a preprocessor by providing the features to our optical neural network classifier. In the next section, we briefly describe the general theory of a conventional JTC and then we extend the discussion to multiple inputs. Next, we provided some experimental results to verify the results of the theory. Finally, we describe how a multiple-input JTC can be used for multiwavelet analysis and propose an architecture that has the same space-bandwidth product as a two-input JTC. Note that all figures for this chapter are at the end of the chapter.

### 4.1 Conventional joint-transform correlator

To perform the correlation operation with a JTC, functions are encoded in the input plane. A schematic diagram of a conventional JTC is shown in Figure 4.1. To perform the cross-correlation between the images  $b(x,y)$  and  $d(x,y)$ , they are centered at  $x = +a$ . A lens produces the Fourier transform when the input plane is illuminated with coherent light. In the Fourier plane, the complex light field is

$$U = B(p,q) e^{j\alpha p} + D(p,q) e^{-j\alpha p}, \quad (4.1)$$

where  $B(p,q)$  is the Fourier transform of  $b(x,y)$ , and similarly for  $d(x,y)$ . A square-law device, such as a liquid crystal light valve, is placed in the Fourier plane before another lens which performs the Fourier transform.

Alternatively, a camera can be used to record the power spectrum and display it on a spatial light modulator (SLM) before the Fourier transform is performed. The output intensity distribution from a square-law detector can be written as

$$|U|^2 = UU^* = [B(p,q) e^{j\alpha p} + D(p,q) e^{-j\alpha p}] [B(p,q) e^{j\alpha p} + D(p,q) e^{-j\alpha p}]^*. \quad (4.2)$$

Multiplying terms, taking the Fourier transform, and grouping terms results in

$$I = b(x,y) \otimes b(x,y) + d(x,y) \otimes d(x,y) + b(x,y) \otimes d(x+2\alpha, y) + d(x,y) \otimes b(x-2\alpha, y), \quad (4.3)$$

in the output plane, where  $\otimes$  indicates the correlation operation. The first two terms are the autocorrelations of the input functions and appear on the optical axis. The third and fourth terms are the cross-correlation between the two input functions and appear at  $x = +2a$  shown in Figure 4.1.

## 4.2 Multiple-input joint transform correlator

We considered a JTC with an arbitrary number of input images arranged along a line. We used the JTC as in Figure 4.1 but considered  $n$  inputs separated by  $a$  in the input plane arranged along the  $x$ -axis as shown in Figure 4.2. The images were labeled  $a_1(x,y)$  to  $a_n(x,y)$ , with the center image labeled as  $a_{(n+1)/2}(x,y)$ . Using this configuration, the complex light field in the Fourier plane was

$$U = A_1(p,q)e^{j\left(\frac{n-1}{2}\right)\alpha p} + A_2(p,q)e^{j\left(\frac{n-3}{2}\right)\alpha p} \dots A_{\frac{n+1}{2}}(p,q) + \dots A_n(p,q)e^{-j\left(\frac{n-1}{2}\right)\alpha p}. \quad (4.4)$$

The output intensity distribution from a square-law detector was written as  $|U|^2 = U \times U^*$ . Multiplying  $n \times n$  terms, taking the Fourier transform, and grouping terms resulted in  $2n - 1$  locations in the output plane where a correlation response would occur. The output plane was described as

$$I = \left[ \sum_{i=1}^n a_i(x,y) \otimes a_i(x,y) \right] + \left[ \sum_{i=1}^{n-1} a_i(x,y) \otimes a_{i+1}(x+\alpha,y) + \sum_{i=1}^{n-2} a_i(x,y) \otimes a_{i+2}(x+2\alpha,y) + \dots \sum_{i=1}^{n-(n-1)} a_i(x,y) \otimes a_{i+(n-1)}(x+(n-1)\alpha,y) \right] + \left[ \sum_{i=1}^{n-1} a_{i+1}(x,y) \otimes a_i(x-\alpha,y) + \sum_{i=1}^{n-2} a_{i+2}(x,y) \otimes a_i(x-2\alpha,y) + \dots \sum_{i=1}^{n-(n-1)} a_{i+(n-1)}(x-(n-1)\alpha,y) \right] \quad (4.5)$$

The first term in brackets in Eq. (4.5) contains the DC terms which is the sum of the autocorrelations of all the input images. The second term in brackets correspond to  $n - 1$  terms to the left of the DC term which are shown in Figure 4.3; each one of these terms is separated by a distance  $\alpha$ . The third term is similar to the second but corresponds to the right of the DC term in Figure 4.3. In addition, the terms on each side of the DC term are the same but rotated by  $\pi$  radians as in a conventional JTC.

### 4.3 Experimental results with the multiple-input JTC

We obtained experimental results to verify the operation of a multiple-input JTC. We used a JTC with an input displayed on film and an optically addressed SLM in the Fourier plane. We used a model SPT-25 optically-addressed SLM operating in a transmissive mode, manufactured by Micro-Optics Technologies Inc. To operate the device, light of 400nm - 500nm is used as write light which is absorbed by a photosensor layer. Light of 600nm - 1100nm is used as the read light that carries the write-light information. A DC bias of 2V - 15V is placed across the device for proper operation.

Our experimental set-up is shown schematically in Figure 4.4. The Argon laser used a 10x microscope objective, 25mm pinhole and  $f = 250$  mm lens in the spatial filter assembly. The filter was a narrowband laser filter centered at 515 nm. Note that this wavelength is outside of the specification of the SLM, but we obtained better results with this line than with the 488nm line of the laser. The illuminating light just before the input plane had a power of 4.0 mW and both Fourier transform lenses had a focal length of  $f = 500$ mm. The He-Ne laser used as the read light of the SLM used a 10x microscope objective, 10mm pinhole and  $f = 250$  mm lens in the spatial filter assembly. The voltage across the SLM was 12.5V.

The input plane consisted of four of the same images as shown in Figure 4.5 where  $\alpha = 1.5$ mm. The images were each labeled as  $f(x,y)$  and substituted into Eq. (4.5); the expected output plane was described schematically as in Figure 4.6. The output plane consisted of a bright spot on the optical axis and four responses on either side. The responses located at distances  $\alpha$  and  $3\alpha$  from the optical axis had the same intensity, as did the responses located at  $2\alpha$  and  $4\alpha$ . The responses at  $\alpha$  and  $3\alpha$  differed from those at  $2\alpha$  and  $4\alpha$  by a factor of two which would correspond to a factor of four if the power spectrum was detected.

The experimental result corresponding to the left half of Figure 4.6 is shown in Figure 4.7. The optical axis corresponding to the center of Figure 4.6 is shown to the far right of Figure 4.7. Two bright spots along the x-axis corresponded to the autocorrelation responses located at distances  $\alpha$  and  $3\alpha$  from the optical axis. Two additional autocorrelations appeared at a distance of  $2\alpha$  and  $4\alpha$  from the optical axis. A profile plot along the x-axis through the autocorrelation peaks is shown in Figure 4.8 where the peaks can be seen more clearly.

## 4.4 Multiwavelet feature extraction

### 4.4.1 Wavelet transform

The wavelet transform has shown to be useful in many areas including that of pattern recognition.<sup>38</sup> The wavelet transform can be thought of as a correlation between a

wavelet and an input signal. The two-dimensional wavelet transform of an image  $f(x,y)$  can be written as

$$W_f(a,b) = \iint f(x,y) w_{ab}^*(x,y) dx dy, \quad (4.6)$$

where  $w_{ab}(x,y)$  is a set of wavelets that are dilated and shifted versions of a wavelet  $w(x,y)$ , where

$$w_{ab}^*(x,y) = \frac{1}{a} w\left(\frac{x-b_x}{a}, \frac{y-b_y}{a}\right), \quad (4.7)$$

where  $a$  is a scale factor and  $b_x$  and  $b_y$  are translations in the  $x$  and  $y$  directions respectively. Because a wavelet can be thought of as a bandpass filter, an image can be viewed in a particular scale or frequency band after cross-correlation with a wavelet. The cross-correlation result is the image corresponding to the frequency band of the wavelet; it is not necessary to perform an additional inverse transform.

To display a version of an input image that corresponds to one wavelet scale using a JTC, one input is the image of interest and the other is the wavelet function.<sup>39</sup> The resulting image then appears at the output of the JTC. Because wavelets have zero mean, this may present a difficulty in the implementation. To remove the DC component from the wavelet function, it was experimentally shown that the wavelet function could be encoded in phase.<sup>24</sup>

To view an image corresponding to more than one frequency band, the image should be cross-correlated with differently scaled wavelets separately. The results of the cross-correlations are summed to produce an image corresponding to multiple frequency bands. If the sum is coherent, then positive and negative contributions to the output image are possible which is necessary for the general case.

#### 4.4.2 Multiwavelet analysis

Under certain conditions the input arrangement in Figure 4.2 could produce a version of an input image corresponding to multiple wavelet scales. We considered an example that produced a version of an input image that corresponded to two wavelet scales. In other words, the output image corresponded to the sum of the cross-correlations of the input image and two different wavelets. To perform this type of operation we referred to Figure 4.2 and set  $n = 5$ , and  $a_3(x,y) = 0$ . We considered the input image  $f(x,y)$  at locations  $a_1(x,y)$  and  $a_2(x,y)$ , so  $f(x,y) = a_1(x,y) + a_2(x,y)$ . Finally, we

set a wavelet corresponding to one scale  $w_1(x,y) = a_4(x,y)$ , and the wavelet at another scale  $w_2(x,y) = a_5(x,y)$  as shown in Figure 4.9.

The response in the output plane was obtained by substituting the appropriate variables in Eq. (4.5), and was represented schematically as shown in Figure 4.11. The third term from the DC is the term of interest here. It was the coherent sum of correlations of the input image and two different wavelets at two different scales. A diagram of the input and output planes for three wavelet scales were shown in Figures 4.10 and 4.12.

In general, a version of an input image corresponding to  $m$  wavelet scales could be produced. A total of  $2m$  inputs are needed,  $m$  replicated input images on one side of the optical axis and  $m$  wavelet images on the other. There would be  $(4m-2)/2$  correlation results appearing on each side of the central autocorrelation peak. The  $m$ th response from the far end on either side would contain the sum of the images at the different scales.

The separation of the input and wavelet images must be far enough apart so that the output images do not overlap. We considered the maximum widths of the input image and wavelet functions to be  $D_i$ , and  $D_w$  respectively, where  $D_i > D_w$ . Assuming the system has unit magnification, then the maximum sizes in the output plane for the input image autocorrelation and input image-wavelet cross-correlations are  $2D_i$ , and  $D_i + D_w$  respectively. In general, it can be seen (from Figure 4.11 for example) that to separate all the output images then the equality

$$\alpha > 1/2 (4D_i) \quad (4.8)$$

must hold. However, we are primarily interested in the off-axis terms which do not include autocorrelations of the input scenes. In addition, the input images are the same and if an object within them moves, they will move together. Therefore, the condition in Eq. (4.8) will correspond to a separation between images in the input plane of

$$\alpha > D_i + 2D_w, \quad (4.9)$$

to avoid overlap in the output plane.

#### 4.4.3 Simulation

To simulate the result we used a Bessel-Gaussian wavelet,<sup>24</sup> that was described as

$$\frac{1}{\sqrt{a}} w\left(\frac{r}{a}\right) = \frac{1}{\sqrt{a}} J_0\left(\frac{r}{a}\right) e^{-\left(\frac{r}{2a\sigma}\right)^2}, \quad (4.10)$$

where  $s$  is related to the width of the bandpass response,  $a$  is the scale factor, and  $r$  is the distance from the origin.

We performed simulations with an image of an airplane  $f(x,y)$  placed into the configuration of Figure 4.9 using a total of 512 x 512 pixels. The image of the plane contained 50 x 50 pixels and  $a$  was set to 50 pixels. For  $w_1(x,y)$  and  $w_2(x,y)$  values of  $a_1 = 0.7$  and  $a_2 = 1.2$  were used respectively. The center portion of the input plane is shown in Figure 4.13 before subtraction of the DC of the wavelet images. Although the input images were placed a distance  $D_i$  apart in violation of Eq. (4.9), the airplanes were separated by a distance of about  $D_i + Dw_1 + Dw_2$ , where  $Dw_1$  and  $Dw_2$  were the width of the wavelet functions.

The power spectrum was shown in Figure 4.14 and the output plane was shown in Figure 4.15 and consisted of nine responses. The three responses consisting of the one along the optical axis, and the ones immediately to the right and left of the optical axis at  $+a$  were autocorrelation responses. They all had large values and overlapped with each other. In addition, they overlapped the responses located  $+2a$  from the optical axis. Therefore, the large spot in Figure 4.15 consisted of five correlation responses and was shown for different values of thresholds in Figure 4.16.

The remaining correlations were the ones of interest and consisted of two on each side of the large central spot. The two remaining responses on the left hand side of Figure 4.15 were expanded and shown in Figure 4.17. The response on the left corresponded to the wavelet with  $a_2 = 1.2$  and the one on the right corresponded to the sum of the wavelets with  $a_1$  and  $a_2$ . Changing  $a_1$  to  $a_1 = 1.0$  changed the response on the right but not on the left as shown in Figure 4.18. A small part of the correlation between the image and the wavelet with associated with  $a_1$  can be seen in the left side of the image.

#### 4.4.4 Implementation

To implement the multiple-input JTC optically a few points must be considered. One is the removal of the DC from the wavelet image. Wavelets have zero mean, so the wavelet image cannot be used directly. One solution is to display the wavelet in phase<sup>24</sup> or use a DC block arrangement.

Because more than one scale of a wavelet is used in our arrangement, both multiple wavelet and multiple input images, one each for every scale of the wavelet used. The most straight forward approach would be to display all images on an SLM and use a single lens in the JTC. Although wavelets and their scales could be changed dynamically, the large space-bandwidth product and size of Fourier transform lens would limit the

number of wavelet scales that could be used. To reduce the restriction on the lens, the input and wavelet portions of the input plane can be split and focused separately each with a Fourier transform lens.<sup>40</sup>

For the input image side, the image needs to be split into multiple images. This could be performed by conventional optics using beam splitters and mirrors. Alternatively, a holographic element could be used to split the input images and possibly include the lens as schematically shown in Figure 4.19. A similar arrangement could be used on the wavelet side. The wavelet itself is fixed and does not move; however, the selection of different wavelet scales, or different wavelets that could be changed dynamically would be desirable. It is possible that a spatially multiplexed hologram could be used. This might be accomplished by a deflection system on the beam that is incident on the holographic element.

## 4.5 Results

We showed how a JTC could be used with multiple input images, and how a multiple-input JTC can be used for multiwavelet analysis of an input image. Using an image and wavelet as inputs, for  $m$  wavelet scales,  $m$  versions of the wavelet and  $m$  copies of the input image need to be generated. The output consisted of  $4m-1$  correlation results, one of which is the desired output. Using holographic elements, the space-bandwidth product of the system can be made the same as for a two-input joint-transform correlator. In addition, the relationship between the wavelet scales can be made independent by increasing the space-bandwidth of the system. Because an output image can be produced that corresponds to multiple wavelet scales, the system is potentially more useful than one that corresponds to a single scale.

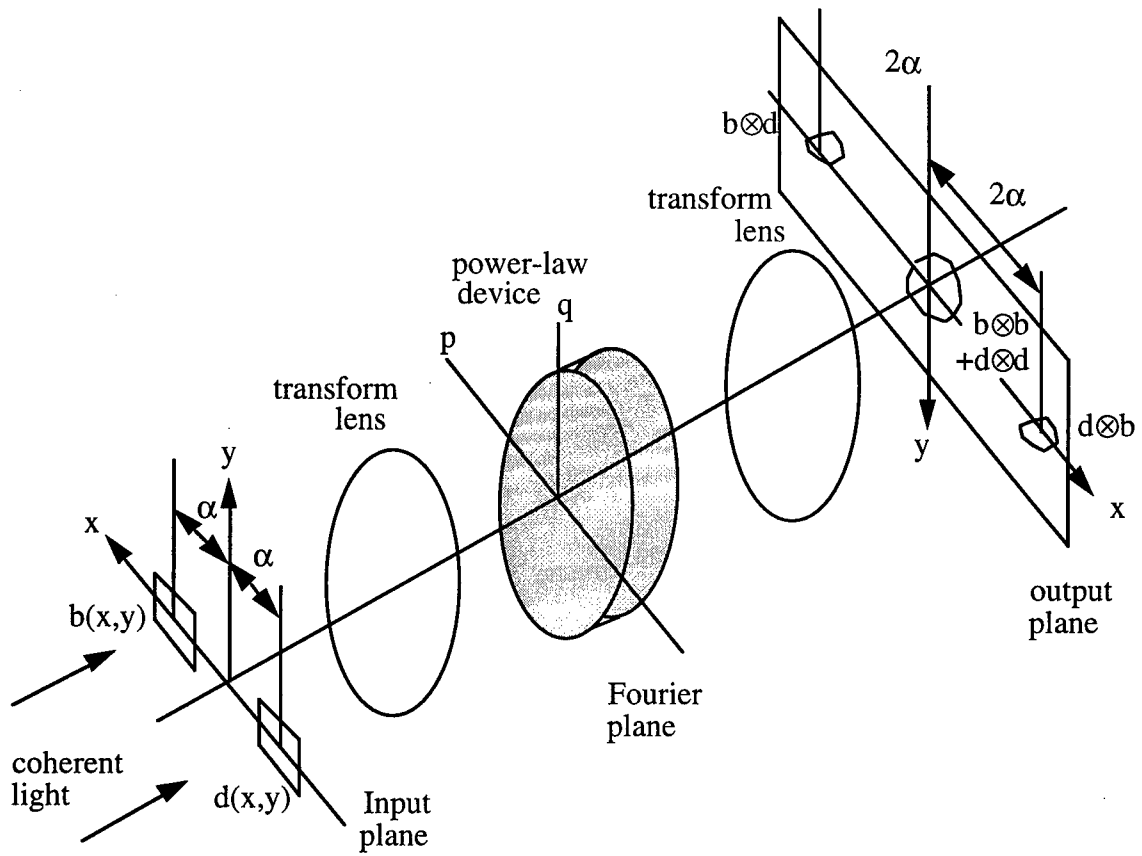


**Figure 4.1:** Schematic diagram of a conventional joint-transform correlator.

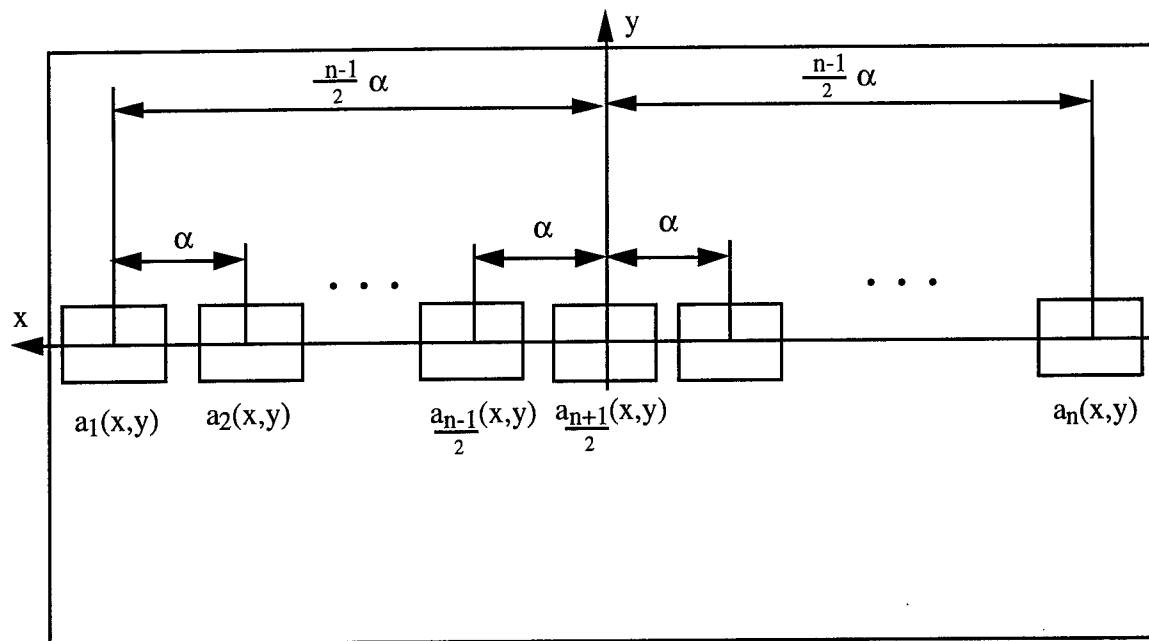


Figure 4.2: Input plane of multiple-input JTC.

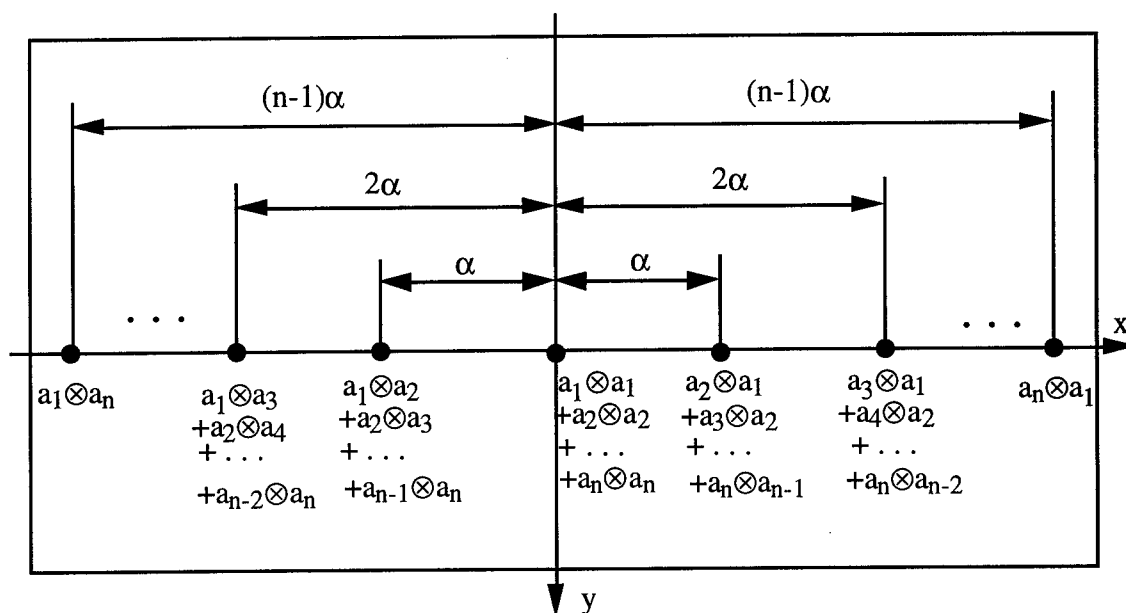
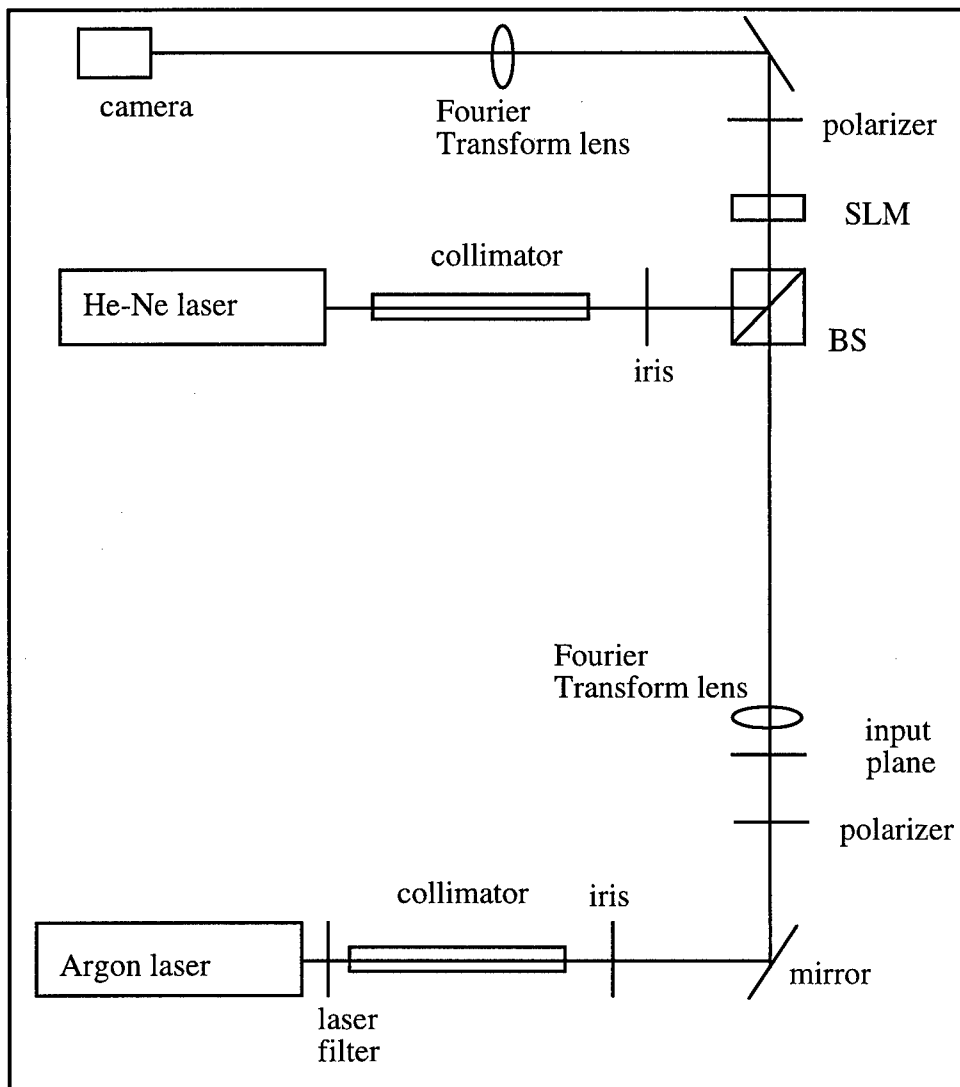
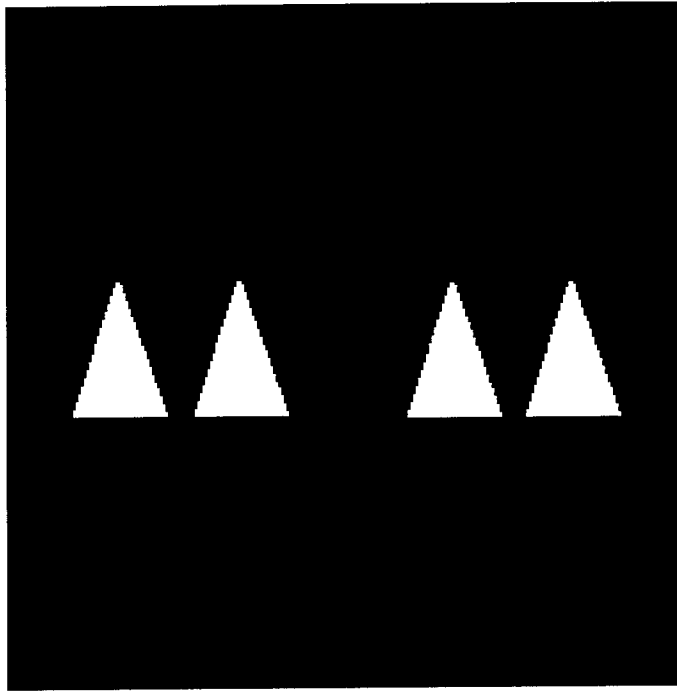


Figure 4.3: Output plane of multiple-input JTC.



**Figure 4.4:** Experimental set-up of multiple input JTC.



**Figure 4.5:** Input image used in experiment.

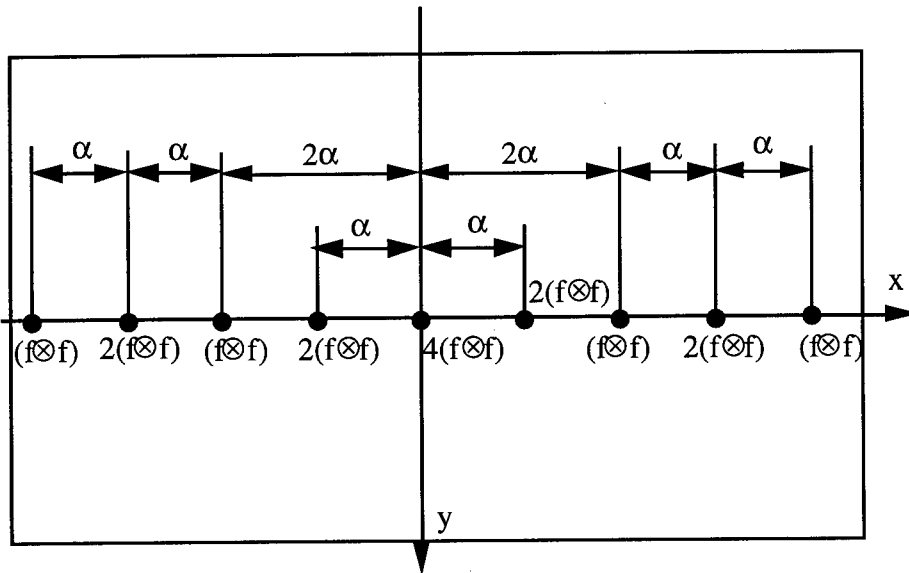


**Figure 4.6:** Input image used in experiment.



**Figure 4.7:** Left hand side of output plane obtained experimentally when Figure 4.5 was used as the input plane intensity distribution.

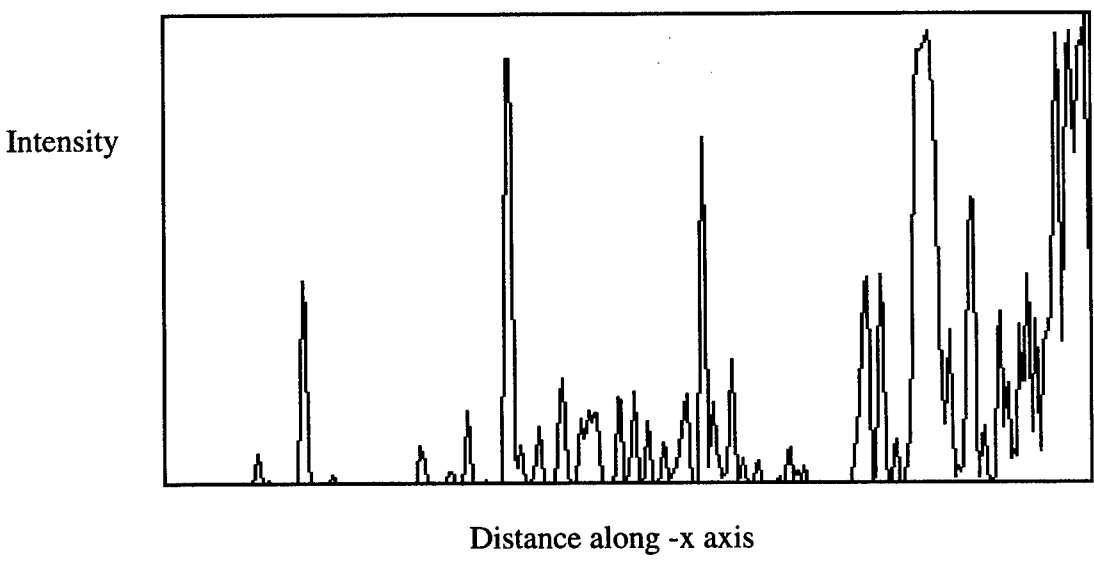


**Figure 4.8:** Left hand side of output plane obtained experimentally when Figure 4.5 was used as the input plane intensity plot of x axis.

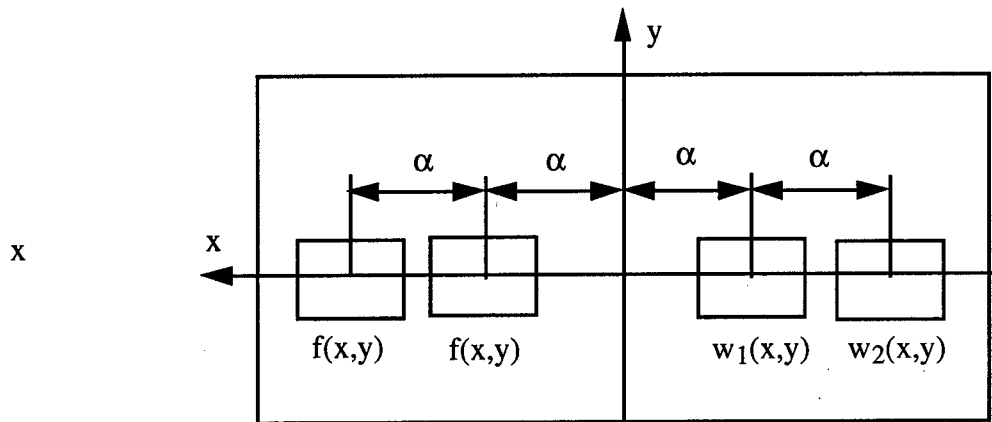


**Figure 4.9:** Input plane for multiwavelet processing two wavelet scales.

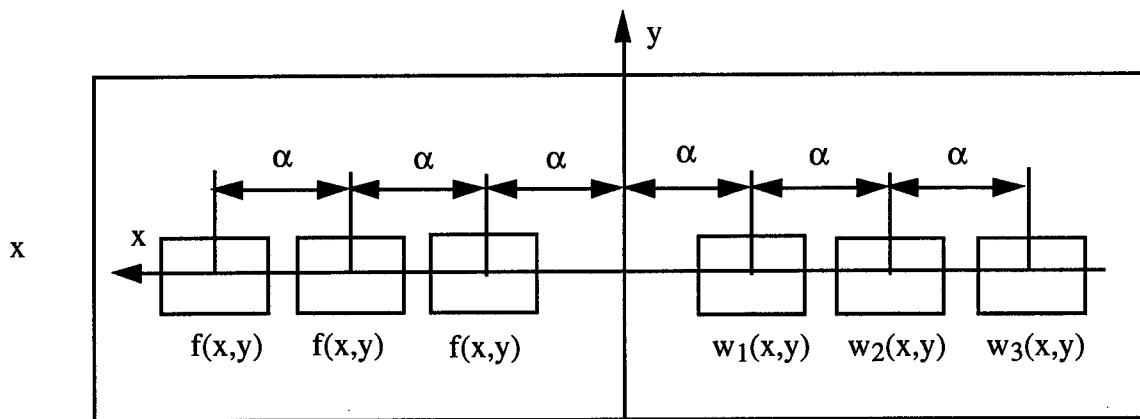


**Figure 4.10:** Input plane for multiwavelet processing three wavelet scales.

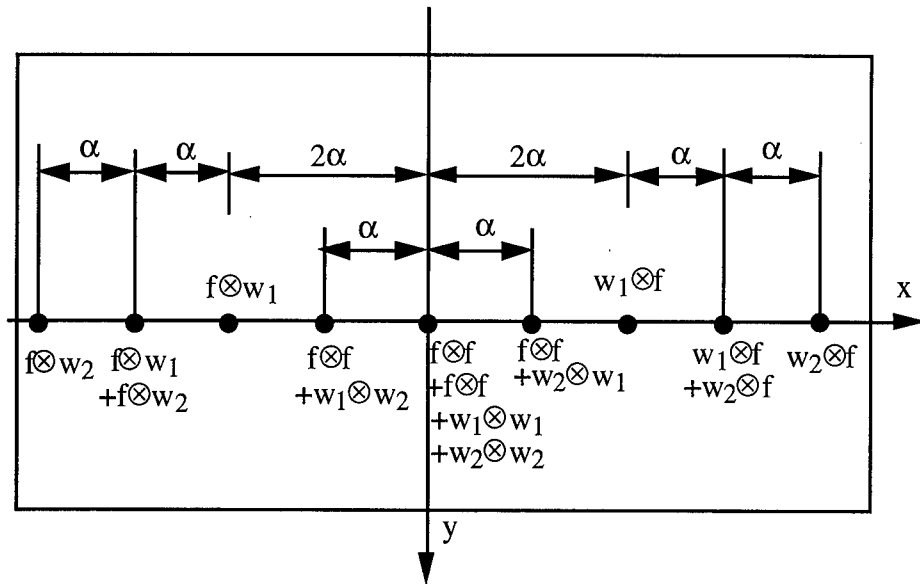


Figure 4.11: Output plane for multiwavelet processing two wavelet scales.

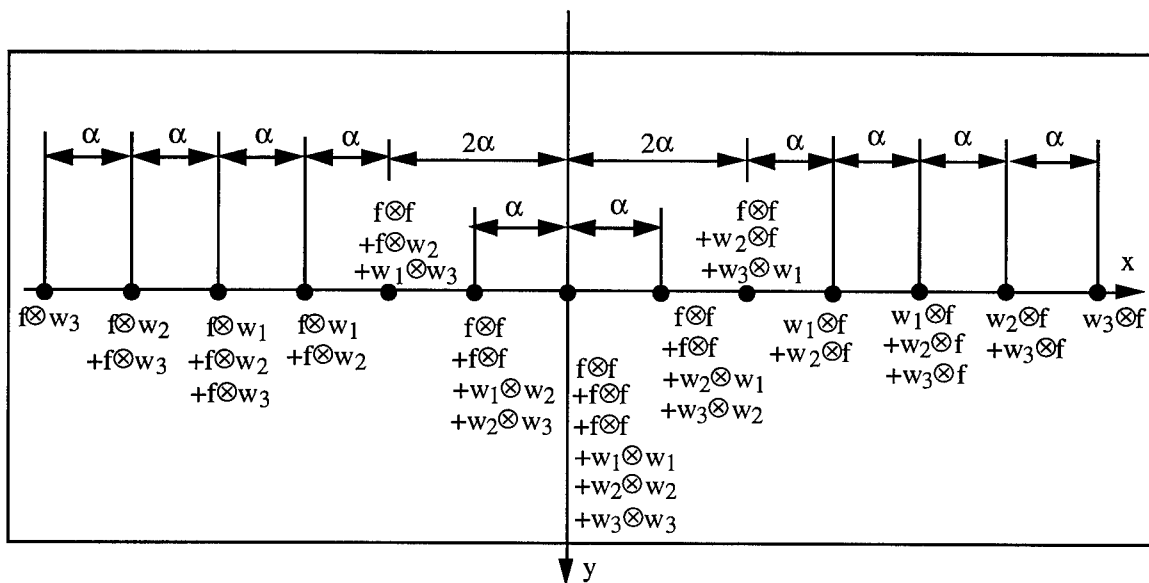
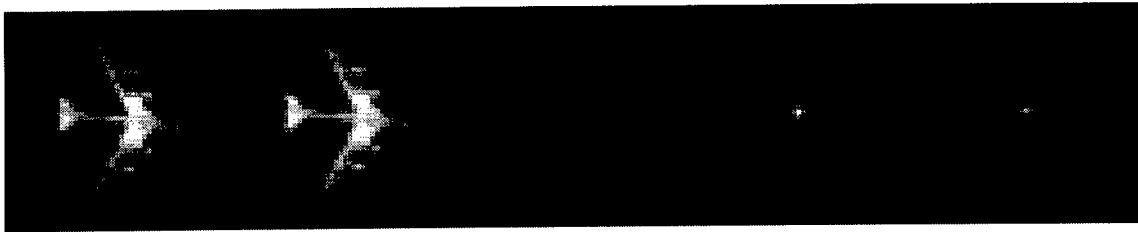
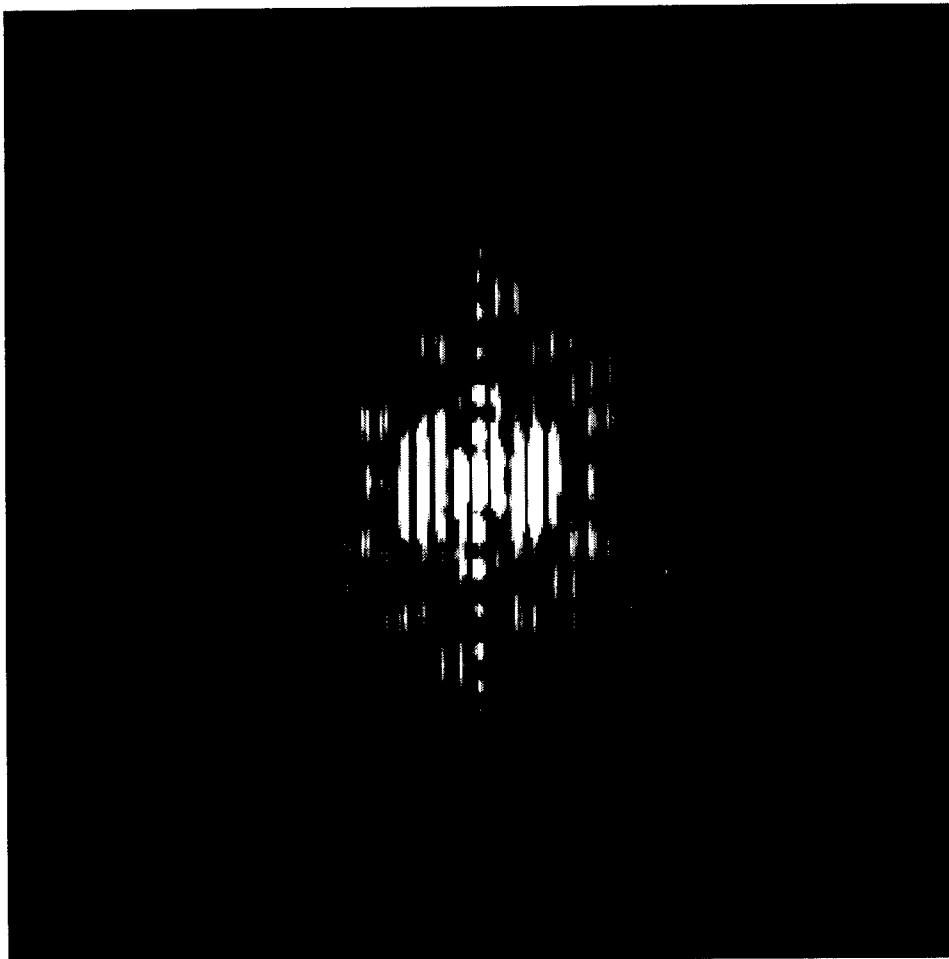


Figure 4.12: Output plane for multiwavelet processing three wavelet scales.



**Figure 4.13:** Center portion of input plane used in simulation experiments.



**Figure 4.14:** Output of multiwavelet simulation power spectrum.

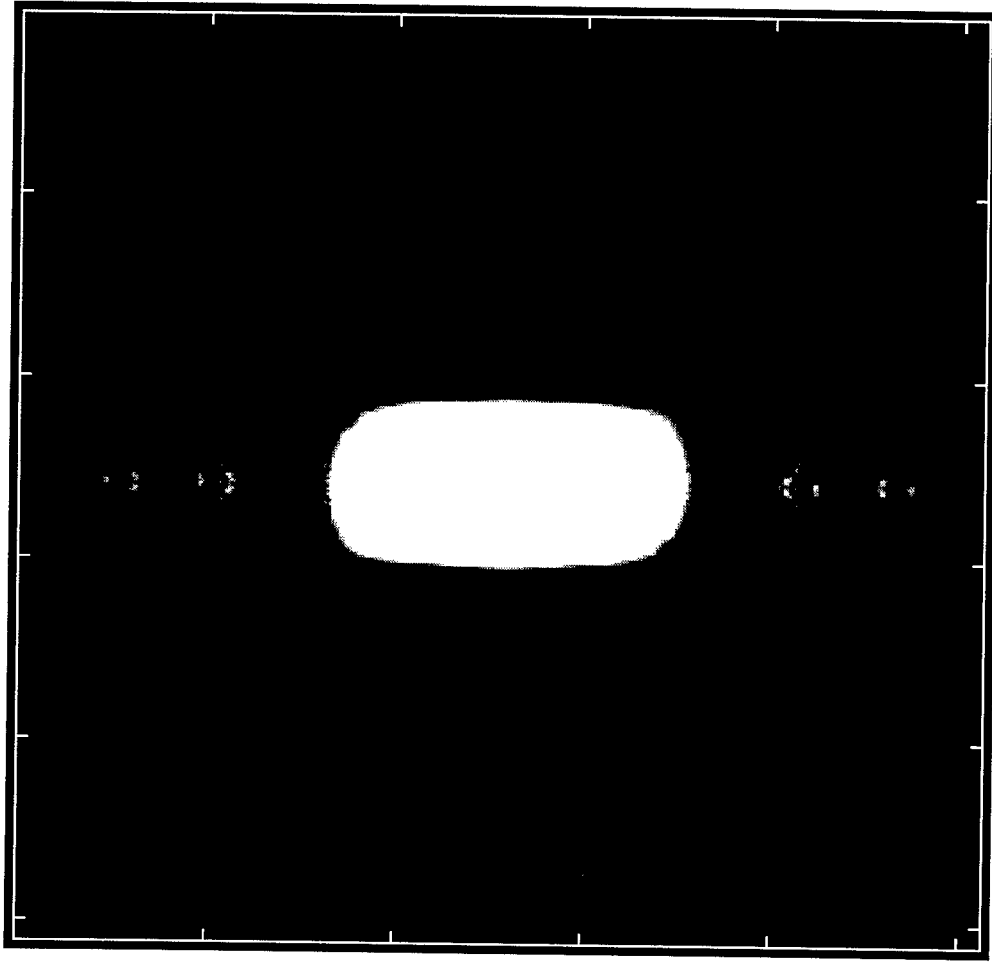


**Figure 4.15:** Output of multiwavelet simulation output plane.

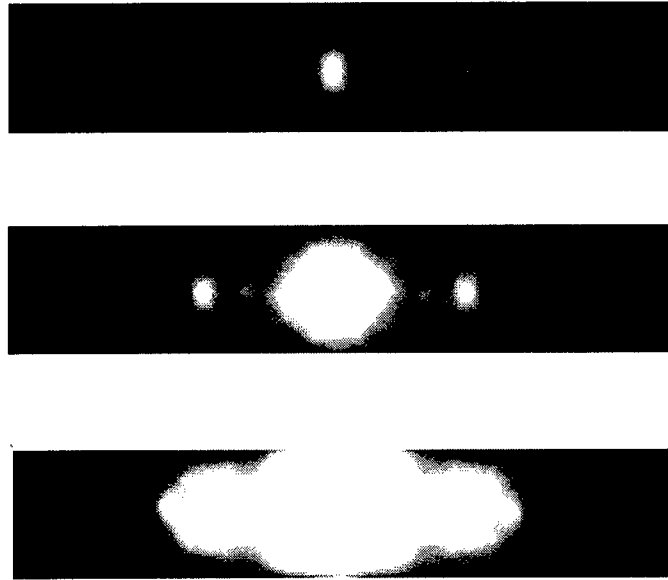


**Figure 4.16:** Center portion of output plane thresholded at three different values showing the overlap of correlation responses.

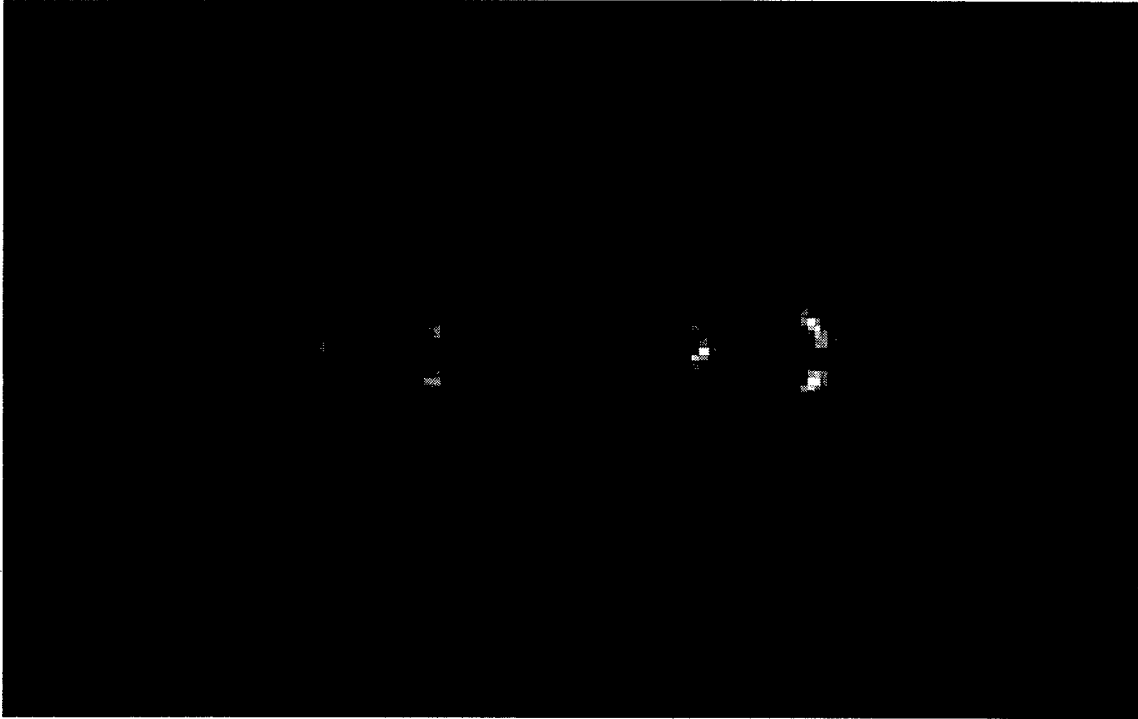


**Figure 4.17:** Close-up view of left hand side of Fig. 11. Response on left is for  $a_2=1.2$ , response on right is for  $a_1 + a_2$ , where  $a_1 = 0.7$ .

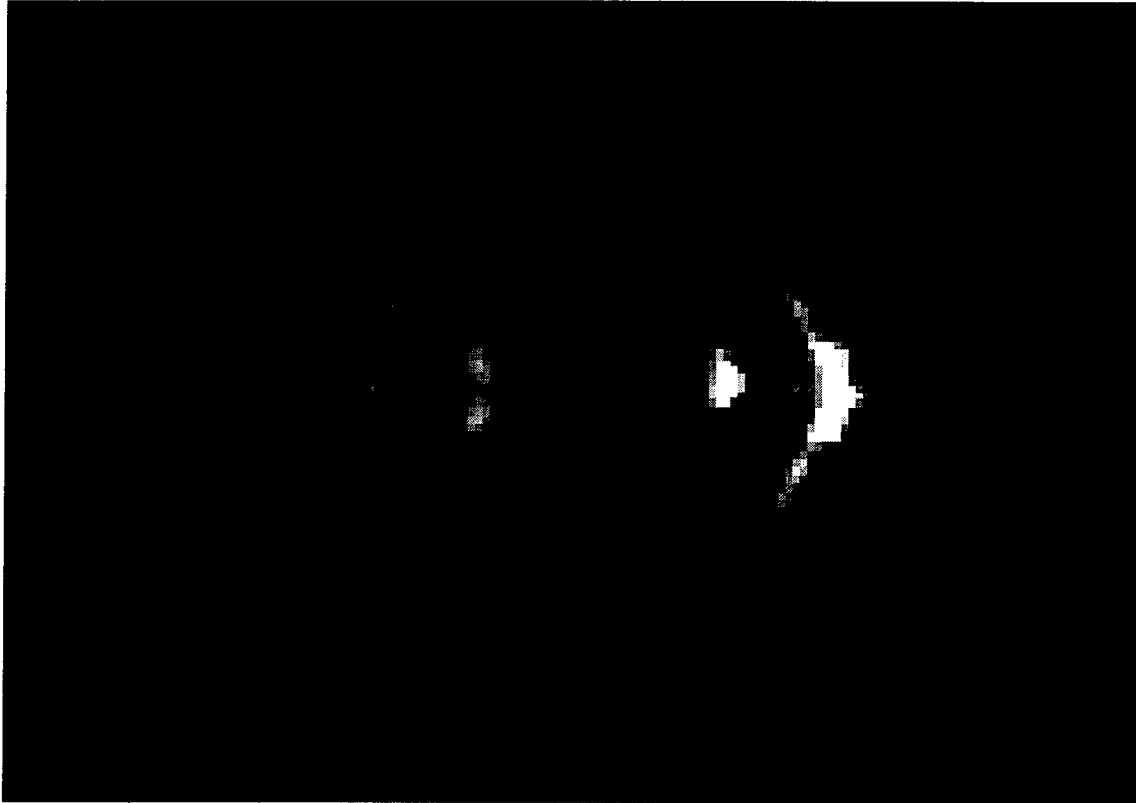


**Figure 4.18:** Close-up view of left hand side of Fig. 11. Response on left is for  $a_2=1.2$  response on right is for  $a_1 + a_2$ , where  $a_1 = 1.0$ .

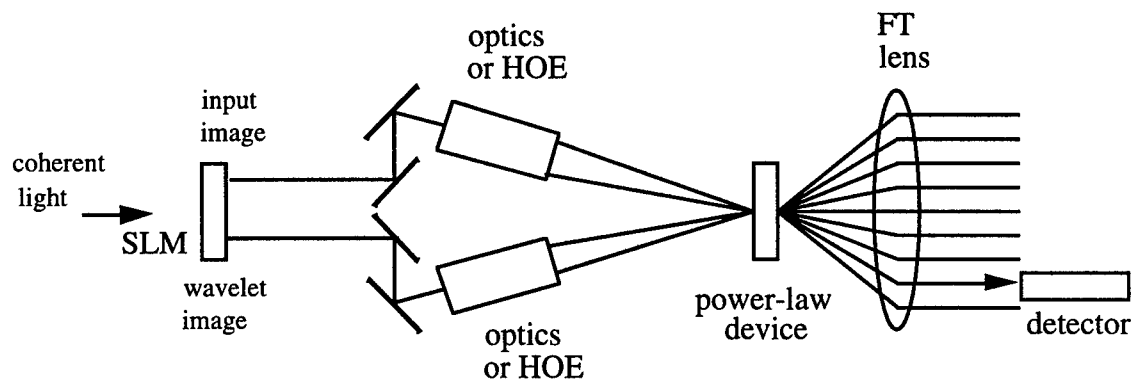


**Figure 4.19:** Schematic diagram of multiple-input JTC used for multiwavelet analysis.

## 5. Conclusion

We have reviewed the theory of radial basis function (RBF) neural networks. We presented a binary-input spatially multiplexed parallel optical system capable of implementing a RBF classifier. The first layer of the neural network was composed entirely of parallel processing optics. The optics compute the Euclidean distances between a 100 bit input vector and 198 centers in parallel. An optical binary-input first layer was demonstrated in a previous project.<sup>31</sup> An electronic postprocessor that implements the second layer of the neural network would have to be fabricated to realize the system's full potential.

We described a design for extending the binary-input adaptive optical RBF neural network classifier to permit analog input signals. This design used a grayscale spatial light modulator (SLM) and replaced the first layer hardware with image subtraction optics. The key component of the image subtraction optics was a variable phase retarder. The retarder was characterized and its phase uniformity changed less than 7% with applied voltage.

The next step in the development of a grayscale classifier would be to obtain and characterize a grayscale SLM. Then, we would develop a computer model and both the variable phase retarder and grayscale SLM parameters would be incorporated into the computer simulations. Finally, the optical portion of the system would be fabricated and compared to the computer model.

We described an optical wavelet transform intended for use as a multi-wavelet image preprocessor for our classifier. The design used an optical joint transform correlator (JTC) to provide cross correlations of multiple input images. We showed experimental results for a JTC which used four input images generated with a spatial light modulator. Using wavelet functions, this multiple-input JTC can be used to perform a multiwavelet analysis of an input image. Using an image and wavelet as inputs, for  $m$  wavelet scales,  $m$  versions of the wavelet and  $m$  copies of the input image need to be generated. The output consisted of  $4m-1$  correlation results, one of which is the desired output. The relationship between the wavelet scales can be made independent by increasing the space-bandwidth of the system. This produces a multiscale output image that corresponds to multiple wavelet scales. This might prove to be more useful than one that corresponds to a single scale.

We characterized critical building blocks of an opto-electronic analog RBF neural network classifier. Future efforts will concentrate on building a analog-input classifier and extending the system further to allow for complex-valued input signals. One of the target applications for this classifier would be the new antenna beamforming approach 'neural beamforming' mentioned in Chapter 1.<sup>14,15,16,17</sup>

The results this project were to be used in a software simulation of the analog-input RBF neural network to determine its feasibility. If feasible the design would have been implemented in hardware. However, this work remains unfinished as this project was canceled due to budget cuts.

## 6. References

- <sup>1</sup> Poggio, T. and Girosi, F., "Networks for Approximation and Learning," *Proc. of the IEEE*, vol. **78**(9), 1481-1497, (1990).
- <sup>2</sup> Poggio, T. and Edelman, S., "A network that learns to recognize three-dimensional objects," *Nature*, vol. **343**, 263-266, 18 Jan 1990.
- <sup>3</sup> Vrckovnik, G. and Carter, C. and Haykin, S., "Radial Basis Function Classification of Impulse Radar Waveforms," *Proc. of IJCNN*, vol. I, 45-50, June 1990.
- <sup>4</sup> Brunelli, R. and Poggio, T., "Face Recognition: Features versus Templates," *IEEE Trans. Patt. Anal. Machine Intell.*, vol. **15**(10), 1042-1052, (1993).
- <sup>5</sup> Arad, N. and Dyn, N. and Reisfeld, D. and Yeshurun, Y., "Image Warping by Radial Basis Functions: Application to Facial Expressions," *CVGIP*, vol. **56**(2), 161-172, (1994).
- <sup>6</sup> Blue, J. L., et al., "Evaluation of Pattern Classifiers for Fingerprint and OCR Applications," *Pattern Recognition*, vol. **27**(4), 485-501, (1994).
- <sup>7</sup> Renals, S. and Rohwer, R., "Phoneme Classification Experiments Using Radial Basis Functions," *Proc. of IJCNN*, vol. I, 461-467, Wash. D.C., June 1989.
- <sup>8</sup> Lee, Yuchun, "Handwritten Digit Recognition Using K Nearest-Neighbor, Radial Basis Function, and Backpropagation Neural Networks," *Neural Computation*, vol. **3**, 440-449, (1991).
- <sup>9</sup> Neifeld, M. A. and Rakshit, S. and Psaltis, D., "Handwritten zip code recognition using an optical radial basis function classifier," In *Proc. of SPIE*, vol. 1469, 250-255, (1991).
- <sup>10</sup> Foor, W. and Neifeld, M. A., "Adaptive optical radial basis function neural network for handwritten digit recognition," *Appl. Opt.*, vol. **34**(32), 7545-7555, (1995).
- <sup>11</sup> Broomhead, D. S. and Lowe, D., "Multivariable Functional Interpolation and Adaptive Networks," *Complex Systems*, vol. **2**, 321-355, (1988).
- <sup>12</sup> Broomhead, D. S., "Signal processing for nonlinear systems," in *Proc. SPIE*, vol. 1565, 228-243, (1991).
- <sup>13</sup> Xu, L. and Krzyzak, A. and Yuille, A., "On Radial Basis Function Nets and Kernel Regression: Statistical Consistency, Convergence Rates, and Receptive Field Size," *Neural Networks*, vol. **7**(4), 609-628, (1994).
- <sup>14</sup> O'Donnell, T. and Simmers, J. and Southall, H., "An Introduction to Neural Beamforming," In *IEEE Dual-Use Technologies and Applications Conference*, vol. I, 483-492, May 1994.
- <sup>15</sup> Simmers, J. and Southall, H. and O'Donnell, T., "Advances in Neural Beamforming," In *Proc. of the 1993 Antenna Applications Symposium*, vol. 1, 203-216, Univ. of Illinois, Sep 1993.
- <sup>16</sup> O'Donnell, T. and Simmers, J. and Jacavanco, D., "Neural Beamforming for Phased-Array Antennas," In *Proc. of the 1992 Antenna Applications Symposium*, vol. 1, 106-115, University of Illinois, Sep 1992.
- <sup>17</sup> Simmers, J. and O'Donnell, T., "Adaptive RBF Neural Beamforming," In *IEEE Command, Control, Communications and Intelligence Technology Applications Conference*, 94-98, June 1992.

- 
- <sup>18</sup> Chen, S. and Grant, P. M. and McLaughlin, S. and Mulgrew, B., "Complex-Valued Radial Basis Function Networks," In *Proc. Third IEE Int'l Conf. Artif. Neural Networks*, 148-152, May 1993.
- <sup>19</sup> Anderson, J. and Platt, J. and Kirk, D., *An Analog VLSI Chip for Radial Basis Functions*, 765-772, Morgan Kaufman, 1993.
- <sup>20</sup> Neifeld, M. A. and Psaltis, D., "Optical implementations of radial basis classifiers," *Appl. Opt.*, vol. **32**(8), 1370-1379, (1993).
- <sup>21</sup> Mallat, S. and S. Zhong, *Wavelet Maxima Representation*, 207-284, Masson and Springer-Verlag, Berlin, (1991).
- <sup>22</sup> S. Weaver, and J. W. Goodman, "A technique for optically convolving two functions," *Appl. Opt.* **5**, 1248-1249 (1966).
- <sup>23</sup> *Real-time optical information processing*, B. Javidi, and J. L. Horner, Eds., Academic Press: San Diego, CA (1994).
- <sup>24</sup> P. S. Erbach, D. A. Gregory, and X. Yang, "Optical wavelet transform by the phase-only joint-transform correlator," *Appl. Opt.* vol. **35**(17), 3117-3126, (1996).
- <sup>25</sup> X. Yang, N. P. Caviris, and M. Wen, "Optical wavelet correlators for cluttered target identification," In *Optical Pattern Recognition V*, SPIE 2237, 402-418, (1994).
- <sup>26</sup> J. Li, Y. Zhang, and J. Hu, "Object recognition with a wavelet-transform-based joint transform correlator," *Opt. Eng.* vol. **35**(3), 775-777, (1996).
- <sup>27</sup> J. Wang, and B. Javidi, "Multiobject detection using the binary joint transform correlator with different types of thresholding methods," *Opt. Eng.* vol. **33**, 1793-1804, (1994).
- <sup>28</sup> M. Deutsch, J. Garcia, and D. Mendlovic, "Multichannel single-output color pattern recognition by use of a joint-transform correlator," *Appl. Opt.* vol. **35**(35), 6976-6982, (1996).
- <sup>29</sup> S. P. Kozaitis, M. A. Getbehead, and W. E. Foor, "Multispectral image feature extraction by the joint wavelet-transform correlator," in *Optical Pattern Recognition VIII*, D. P. Casasent, Ed., Proc. SPIE 3073, paper 34, (1997).
- <sup>30</sup> Foor, W. E., "Adaptive Optical Radial Basis Function Neural Network Classifier," Rome Laboratory Technical Report RL-TR-94-239, December 1994.
- <sup>31</sup> Foor, W. E., Getbehead, M. A., and Rosetti, J. B., "Adaptive Optical Neural Network Classifier Systems," Rome Laboratory Technical Report RL-TR-97-122, May 1997.
- <sup>32</sup> Neifeld, M. A., Rakshit, S., Yamamura, A., Kobayashi, S., and Psaltis, D., "Optical disk implementation of radial basis classifiers," In *Proc. of SPIE*, vol. 1347, 4-15, (1990).
- <sup>33</sup> Ebersole, J. F., "Optical Image Subtraction," *Opt. Eng.*, vol. **14**(5), 436-447, (1995).
- <sup>34</sup> Gabor, D., Stroke, G. W., Restrict, R., Funkhouser, A., and Brumm D., "Optical Image Synthesis (Complex Amplitude Addition and Subtraction) by Holographic Fourier Transformation," *J. Opt. Soc. Am.*, vol. **60**(8), 1037-1041, (1970).

---

<sup>35</sup> Lee, S. H., Yao, S. K. and Milnes, A. G. , "Optical Image Synthesis (Complex Amplitude Addition and Subtraction) in Real Time by a Diffraction-Grating Interferometric Method," *J. Opt. Soc. Am.*, vol. **60**(8), 1037-1041, (1970).

<sup>36</sup> Marom, E., "Real-time image subtraction using a liquid crystal light valve," *Opt. Eng.*, vol. **25**(2), 274-276, (1986).

<sup>37</sup> Liu, H. K. and Chao, T. H", "Optical Image Subtraction Techniques," 1975--1985, in *Proc. SPIE*, vol. 638, pp. 55-65, 1986.

<sup>38</sup> M. B. Ruskai, B. Beylkin, R. Coifman, I. Daubechies, S. Mallat, Y. Meyer, and L. Raphael, *Wavelets and Their Applications*, Jones & Bartlett: Boston, MA, (1992).

<sup>39</sup> W. Wang, G. Jin, Y. Yan, and M. Wu, "Joint wavelet-transform correlator for image feature extraction," *Appl. Opt.* vol. 34(2), 370-376, (1995).

<sup>40</sup> T. C. Lee, et al., "Dual-axis joint-Fourier-transform correlator," *Opt. Lett.* vol. 4, 121-123, (1979).